Impact of Convectively Generated Low-Frequency Gravity Waves on Evolution of Mesoscale Convective Systems

Rebecca D. Adams-Selin*

Atmospheric and Environmental Research, Inc.

**Corresponding author address:* Atmospheric and Environmental Research, 11515 South 39th St, Suite 102, Bellevue, NE 68123

E-mail: rselin@aer.com

Early Online Release: This preliminary version has been accepted for publication in *Journal of the Atmospheric Sciences*, may be fully cited, and has been assigned DOI 10.1175/JAS-D-19-0250.1. The final typeset copyedited article will replace the EOR at the above DOI when it is published.

ABSTRACT

Accepted for publication in *Journal of the Atmospheric Sciences*. DOI10.1175/JAS-D-19-0250.1.

Idealized numerical simulations of Mesoscale Convective Systems (MCSs) over a range of instabilities and shears were conducted to examine low-frequency gravity waves generated during initial and mature stages of convection. In all simulations, at initial updraft development a first-order wave was generated by heating extending the depth of the troposphere. Additional first-order wave modes were generated each time the convective updraft reintensified. Each of these waves stabilized the environment in advance of the system. As precipitation descended below cloud base, and as a stratiform precipitation region developed, second-order wave modes were generated by cooling extending from the mid-levels to the surface. These waves destabilized the environment ahead of the system but weakened the 0-5 km shear. Third-order wave modes could be generated by mid-level cooling caused by rear inflow intensification; these wave modes cooled the mid-levels destabilizing the environment. The developing stage of each MCS was characterized by a cyclical process: developing updraft, generation of $n = 1$ wave, increase in precipitation, generation of $n = 2$ wave, and subsequent environmental destabilization reinvigorating the updraft. After rearward expansion of the stratiform region, the MCSs entered their mature stage and the method of updraft reinvigoration shifted to absorbing discrete convective cells produced in advance of each system. Higher-order wave modes destabilized the environment making it more favorable to development of these cells and maintenance of the MCS. As initial simulation shear or instability increased, the transition from cyclical wave/updraft development to discrete cell/updraft development occurred more quickly.

Accepted for publication in *Journal of the Atmospheric Sciences*. DOI10.1175/JAS-D-19-0250.1.

1. Introduction

Gravity waves generated by convection are widely understood to impact the environment surrounding that convection. Vertical motions associated with these waves can act to both initiate (e.g., Wilson et al. 2018) or organize (Bretherton and Smolarkiewicz 1989; Nicholls 1991; Pandya et al. 1993; Mapes 1993; Shige and Satomura 2001; Liu and Moncrieff 2004) convection. Convectively-generated gravity waves fall along a spectrum of high to low frequency; depending on the frequency the waves have different sets of causal factors and subsequent impacts. In a resting atmosphere, wave frequency is related to wave energy propagation direction through

$$\cot(\alpha) = \frac{\omega}{\sqrt{N^2 - \omega^2}} \tag{1}$$

where α is the angle of energy propagation as measured from the vertical, N is the Brunt-Väisälä frequency, and ω is the frequency of the wave (Pandya et al. 2000). According to (1), as the wave frequency decreases the direction of energy propagation becomes more horizontal. Low-frequency waves thus can propagate horizontally for extended distances without their energy escaping vertically. These waves are mainly excited by changes in the diabatic heating profile associated with convection (Lane and Reeder 2001; Pandya et al. 2000). High-frequency waves, conversely, lose most of their energy to vertical propagation unless a trapping mechanism exists. They are generally excited by cyclical re-development of convective cells (McAnelly et al. 1997, MNCN97 hereafter) or nonlinear advection of buoyancy (Lane and Reeder 2001). High- and low-frequency waves can work in concert to develop or organize convection, a process termed "discrete propagation (Fovell 2002; Fovell et al. 2006; Su and Zhai 2017): low-frequency waves prepare the environment through more gentle ascent over a larger area, while high-frequency waves actually initiate the convection. Low-frequency waves have also been shown to aid environmental recovery from previous convection through subsequent destabilization (Trapp and Woznicki 2017).

Accepted for publication in *Journal of the Atmospheric Sciences*. DOI10.1175/JAS-D-19-0250.1.

Low-frequency wave structure is defined by vertical modes of diabatic heating. These modes also determine its speed through

$$c = \frac{NH}{n\pi} \tag{2}$$

where c is the wave speed, H the vertical depth of the troposphere, and n the vertical mode of the diabatic heating profile (Nicholls 1991). Here an $n = 1$ wave would be generated by an increase in heating over the depth of the troposphere peaking at the midlevels, roughly corresponding to the heating profile in the convective region of an MCS (Gallus and Johnson 1991). The wave itself consists of a wave front with descent over the depth of the troposphere that propagates away from the heating source at speed c, shown in Fig. 1a. The displacement and warming resulting from the descent were found by Mapes (1993) to be "semi-permanent" until the diabatic heating profile decreases, at which time a wave front of ascent through the depth of the troposphere would be generated (Fig. 1a). Lane and Zhang (2011) noted the cyclical nature of heating within convection as cells redevelop; when using a heating profile periodic in time they found $n = 1$ waves can travel in downdraft/updraft couplets. Adams-Selin and Johnson (2013) observed four $n = 1$ updraft/downdraft couplets using Oklahoma Mesonet surface pressure data, and Su and Zhai (2017) similarly observed a $n = 1$ couplet. Microphysical heating aloft and cooling over the lower half of the troposphere, the heating profile of an MCS stratiform region (Gallus and Johnson 1991; Fovell 2002), generates $n = 2$ wave modes with ascent over the lower half of the troposphere; $n = 3$ wave modes can be associated with ascent in either the lower or middle third of the troposphere. Lane and Reeder (2001) found the impact of these waves on the surrounding convective available potential energy (CAPE) and convective inhibition (CIN) fields varied; waves with upward vertical motions maximized in the lower (middle) troposphere most impacted CIN (CAPE) fields.

Low frequency waves thus are expected to be produced by Mesoscale Convective Systems (MCSs), but to this point there has been no systemic examination of waves produced during an

Accepted for publication in *Journal of the Atmospheric Sciences*. DOI10.1175/JAS-D-19-0250.1.

MCS lifecycle. Recent research has noted the prevalence of bores associated with nocturnal MCSs, particularly in the Great Plains region of the United States. Efforts have examined how bores can maintain lifting within, and destabilize large regions in advance of, MCSs through low-level lifting (Haghi et al. 2017; Johnson et al. 2018; Parsons et al. 2019; Zhang et al. 2020). The development of the nocturnal low-level jet often leads to a critical layer to trap wave energy (Lindzen and Tung 1976; Koch et al. 1991) and a flow regime favorable to bores (Rottman and Simpson 1989; Haghi et al. 2017). It is likely that low-frequency gravity waves occur concurrently with bores. Parsons et al. (2019) and Haghi et al. (2019) both suggest such a possibility but thus far the low-frequency gravity waves associated with MCSs have not yet been identified. MCSs also frequently initialize in a weakly stable or neutral temperature regime before sunset, where bores are not as frequent but low-frequency waves could still occur. While it is possible for the elevated stable and trapping layers necessary for long-lived bores to exist during the day (e.g., Fig. 1 of Zhang et al. (2020)), the existence of such a vertical temperature profile is not guaranteed.

Thus, given the established importance of low-frequency gravity waves in "preparing"' the surrounding environment for additional convective development and initiation, a systematic examination of low-frequency gravity waves produced during the lifetime of an MCS is necessary. This work will focus on the waves generated by a Mesoscale Convective System (MCS), the specific modes produced by the different stages of its lifecycle, and how those wave modes vary across a range of environments. Previous studies such as Pandya and Durran (1996) and Pandya et al. (2000) have examined how different vertical tilts of the heating profile have impacted the circulation within an MCS, but have not studied how different initial environments modify the in-storm latent heating distributions. It is hypothesized that these the low-frequency waves produced by MCSs vary among storms occurring in different environments, subsequently impacting the waves'

Accepted for publication in *Journal of the Atmospheric Sciences*. DOI10.1175/JAS-D-19-0250.1.

environmental effects surrounding the MCS, additional convective development, and potential discrete propagation.

The methodology and configuration of the simulations are described in Section 2. The control run is described in Section 3. Generated wave and impact sensitivities to environmental shear and instability variations are discussed in Sections 4 and 5. The MCS response across the sensitivity tests is described in Section 6. Discussion and conclusions are presented in Section 7.

2. Methodology

Idealized Cloud Model 1 version 18 (CM1; Bryan and Fritsch 2002) simulations were used. This study expands upon previous examinations of low-frequency gravity waves that used simplified linearized models with specified heat sources (e.g., Bretherton and Smolarkiewicz 1989; Nicholls 1991; Pandya et al. 1993; Mapes 1993; Liu and Moncrieff 2004) by incorporating all attendant non-linear effects. Stechmann and Majda (2009) found such effects to be important when determining wave responses in environments with non-zero wind shear. Nine sets of initial conditions were defined using a modified version of the sounding from Weisman and Klemp (1982), three different thermodynamic profiles and three different shear profiles. For each profile, N was calculated and smoothed if anywhere in the profile was discontinuous below the tropopause to ensure no trapping levels were present to confuse the results. In all profiles, the only smoothing of N that was required was below 2 km around the height of the lifted condensation level. Once N was smoothed, a new potential temperature was solved for, assuming q_v was unmodified from the original sounding.

A 350 km (x direction) by 300 km (y direction) by 18 km (z direction) domain was used with open-radiative lateral boundary conditions and zero-flux lower and upper boundary conditions. The horizontal grid-spacing was 250 m and the vertical grid spacing was uniformly 100 m. A time

Accepted for publication in *Journal of the Atmospheric Sciences*. DOI10.1175/JAS-D-19-0250.1.

step of 1.5 s was used with vertically implicit Klemp-Wilhelmson time-splitting with an acoustic time step of 1/3 s. Rayleigh damping was applied above 14 km with an inverse e-folding time of 1/300 s^{-1}. The simulation parameterized subgrid turbulence via a prognostic TKE scheme (Bryan and Fritsch 2002). Convection was initialized via the "cold pool-dam break" method (Weisman et al. 1997), consisting of a rectangular box of negative potential temperature perturbation established during initiation. The cold perturbation of -6 K extended from 0 to 100 km in the x direction, from 50 to 250 km in the y direction, and linearly decreased until 0 K at 2.5 km aloft. The Morrison microphysical parameterization (Morrison et al. 1997) was used with the hail option.

The background stability and shear of the initiating environment were varied systematically to examine its impact on the waves produced. Three different surface mixing ratio (q_v) values were used of 12.2, 14.3, and 16.2 g kg^{-1}, resulting in three different initial Maximum Unstable Convective Available Potential Energy (MUCAPE) values of approximately 1500, 2500, and 3500 J kg^{-1}. (Because the convection was surface-based, however, all further analyses of CAPE will use a surface-based value.) Shear profiles were linear with easterly winds at the surface of 5, 15, and 25 m s^{-1} decreasing to 0 m s^{-1} at 5 km aloft; no trapping or critical levels exist in the shear profile. These perturbations were designed to mimic those of Weisman and Klemp (1982) and Weisman et al. (1988) to allow for comparison with the results of those studies. Two additional simulations were run to test the sensitivity of results to the initialization method and addition of a nocturnal boundary layer. All simulations run are listed in Table 1.

3. Control simulation

The control simulation, 14.3H15 (Fig. 2), has 15 m s^{-1} of 0-5 km shear, a surface q_v of 14.3 g kg^{-1}, 2497 J kg^{-1} of MUCAPE, and the profile most similar to the original Weisman and Klemp (1982) sounding. Simulated radar reflectivity values first become apparent at 20 minutes

Accepted for publication in *Journal of the Atmospheric Sciences*. DOI10.1175/JAS-D-19-0250.1.

into the simulation as a convective updraft extends through the mid-levels in a north-south line. Precipitation first reaches the surface at 24 minutes (Fig. 2c). The convective line widens and a small region of leading stratiform precipitation develops around 35 minutes, which transitions to a leading line-trailing stratiform configuration by 54 minutes (Fig. 2f). As the stratiform region extends rearward, a rear inflow jet develops and slowly spreads westward. An intensification of the rear-to-front flow occurs just prior to 100 minutes (Fig. 2i). By 90 minutes discrete convective cells have formed in advance of the main updraft (Fig. 2h). At 115 minutes these cells were absorbed into the main updraft, reinvigorating it.

Unlike previous studies of low-frequency gravity waves forced by idealized heat sources, the highly variable nature of the latent heating profile within a full MCS simulation will result in many gravity waves of a range of frequencies (e.g., Adams-Selin and Johnson 2013). Identifying specific wave modes is therefore difficult. In this study, the existence of a specific wave mode is confirmed provided its phase speed and a subsequent Fourier decomposition method agree. That wave mode must also be reflected within the vertical motion field for the remaining length of the simulation once generated to ensure the waves are low frequency.

a. Fast-moving wave mode

Three waves of mode $n = 1$ consisting of downdraft-updraft couplets are evident in the vertical wind field within a Y cross-section at 6 km aloft (Fig. 3a). The waves associated with downward motion are marked by solid lines, and with upward motion by dashed lines. Vertical motion associated with $n = 1$ waves should peak in the mid-levels. The motions associated with these waves at 2.5 km are still evident but not as strong (Fig. 3b). The three waves propagate quickly away from the initiating convection at similar speeds of 36.6, 35.9, and 34.0 m s^{-1} after accounting for the mean tropospheric u wind, calculated from the initial wind profile, of -1.9 m s^{-1}. With a

Accepted for publication in *Journal of the Atmospheric Sciences*. DOI10.1175/JAS-D-19-0250.1.

mean N of 9.8E-3 s^{-1} the predicted $n = 1$ wave speed from (2) is 37.4 m s^{-1}. Figures 2a and b show an increase in mid-level latent heating between 14 and 20 min, highlighted by the horizontal black arrow. Generation of an $n = 1$ gravity wave follows at 20 min (Fig. 2c) consisting of upward vertical motion extending the depth of the troposphere that propagates away from the system. A subsequent lessening of mid-level heating is evident at 30 min (Fig. 2d). The resulting $n = 1$ response is difficult to see in Fig. 2d due to the strength of a concurrent $n = 2$ wave, but it is visible in Fig. 3a.

b. Slow-moving wave modes

Three slower-moving waves are visible 2.5 km aloft in Fig. 3b. These waves appear to be higher order modes than the $n = 1$ waves due to their slower speed. The first wave is associated with upward vertical motions more evident at 2.5 km although still visible at 6 km. The wave moves at a speed of 15.6 m s^{-1} accounting for the mean tropospheric u wind, approximately half the speed of the second $n = 1$ wave or 17.9 m s^{-1} and agreeing with (2). Figures 2b,c shows an increase in low-level latent cooling associated with the first descent of precipitation below cloud level, indicated by the horizontal black arrow in Fig. 2c. The $n = 2$ vertical motion response, upward motion in the lower half of the troposphere overlaid by downward motion aloft, can be seen in Fig. 2d shortly ahead of the convective updraft and again in Fig. 2e at X=115 km having propagated ahead of the system.

The second higher order wave in Fig. 3b similarly shows stronger upward motions at 2.5 km than at 6 km. In Fig. 2g, a second $n = 2$ wave is evident in the vertical motion field at X=112 km. Prior to the appearance of this wave, the latent cooling field increases from the surface to 6 km in Fig. 2f (noted by the horizontal arrow). This wave moves at 15.3 m s^{-1}, similar to the first $n = 2$ wave.

Accepted for publication in *Journal of the Atmospheric Sciences*. DOI10.1175/JAS-D-19-0250.1.

The third wave does have upward motions at 2.5 km, but the upward motion at 6 km appears stronger. The wave moves at a slower speed of 13.7 m s^{-1}, closer to one-third of the initial $n = 1$ wave speed (12.2 m s^{-1}). Figure 2i shows an increase in latent cooling from 3 to 6 km just prior to 100 min, generation time of this wave. Unfortunately an ongoing discrete propagation event prevented identification of an $n = 3$ wave in cross-sections of vertical motion, but the change in vertical peak cooling location as well as the slower speed hints strongly at this feature being an $n = 3$ wave. Additional analysis will take place in the next subsection.

The cold pool-dam break initialization method is a dynamically forceful method of forcing convection. Thus it is of interest to determine if the waves generated here are artifacts of that initialization method. The 14.3H15 simulation was repeated with identical initialization conditions except use of a line of three warm bubbles for convective initialization. While the forward propagation speed was not as large, likely due to an initially smaller cold pool, timing of wave activity was very similar (Fig. 4a,b). In Fig. 4a,b, the solid, dashed, and dotted lines are copied from the $n = 1$, $n = 2$, and $n = 3$ wave fronts identified in the control simulation (Fig. 3) yet align almost exactly with the waves produced in the bubble-initialized simulation.

The environment used here was specifically designed to not allow bore generation to mimic initialization of MCSs during daytime. In order to examine if similar low-frequency waves develop when initialized in a nocturnal environment, a simulation was run with the same shear profile, but with the surface temperature cooled by 6 K and the temperature profile up to 1 km was defined using $T = min(T, T_{sfc})$ (the artificial cooling method of Parker 2008). Similar $n = 1, 2, 3$ waves are generated in Figs. 4c,d, showing these wave processes will occur in both daytime and nocturnal MCSs.

Accepted for publication in *Journal of the Atmospheric Sciences*. DOI 10.1175/JAS-D-19-0250.1.

c. Generating processes

Each of the waves observed above appeared to be generated in conjunction with changes in the latent heating profile. To evaluate the connection between the latent heating changes and the generated waves, the mean vertical heating and cooling profiles, shown in Fig. 5, were first smoothed with a 1-2-1 filter and then decomposed into 10 Fourier components similar to Stephan et al. (2016). Specifically,

$$S(z) = \sum_{n=1}^{n=10} A_n \sin \frac{\pi n z}{H} \tag{3}$$

where A_n is the coefficient associated with each component, z is height, and and n and H are as in (2). Each component consists of a sine mode with nodes at the surface and at height H. An A_1 coefficient is associated with an $n = 1$ mode, and the values of the coefficient are plotted in black in Fig. 5. It is only plotted if both the coefficient is determined to be 99% significant per a two-tailed t-test, and the entire decomposition is determined to be 99% significant per the F-statistic. The coefficients A_2 and A_3 are plotted in Fig. 5b. Coefficient A_4 is only rarely significant; waves associated with any higher coefficients would not propagate quickly enough to be seen or modify the environment ahead of the convective line.

Figure 5a also shows the maximum vertical motion in the cross-section at 6 km, plotted in white. From these two line plots, it is evident that the A_1 coefficient and mid-level updraft speed are correlated, as would be expected. The cyclical nature of the updraft, at least prior to 70 min, can be seen, with peaks in mid-level heating and updraft speed followed by times of diminished heating and slower updrafts. The downward motion portion of each $n = 1$ wave couplet is generated when, or shortly after, a peak in the A_1 coefficient occurs; the upward motion portion when a minimum in the A_1 coefficient occurs. In this way the $n = 1$ wave couplets appear connected to cyclical convective updraft development (similar to MNCN97, Lane and Zhang 2011). It is possible there

Accepted for publication in *Journal of the Atmospheric Sciences*. DOI10.1175/JAS-D-19-0250.1.

are additional $n = 1$ waves generated after 70 min, and the variations in the A_1 coefficient would seem to indicate that could be occurring. However, at that point the vertical motion field ahead of the convective line is complex and identifying additional $n = 1$ waves wasn't possible.

The processes generating the higher order wave modes are more complicated. The first and second $n = 2$ waves are generated shortly after large decreases in the A_2 coefficient (Fig. 5b). From Figs. 2b and c the increase in low-level cooling occurs as precipitation first falls below the cloud and reaches the surface, evidenced by the thick black line enclosing total condensate descending to the surface in Fig. 2c along with an increase in latent cooling in the same location (identified by horizontal arrow). The second $n = 2$ wave occurs shortly after the stratiform precipitation region begins to develop and expand rearward. Figures 2e, f display this process. The horizontal arrow in each subfigure starts at the same location, but in Fig. 2f the total condensate contour has expanded about 5 km rearward. The associated latent cooling deepens and expand upward in the time between the two subfigures. The deeper layer of cooling can also be seen in Fig. 5b. While an additional surge of cooling is evident at 80 min in Fig. 5b, the A_2 coefficient does not decrease as much as during the generation of the two $n = 2$ waves.

The third slow-moving wave, or $n = 3$ wave, is generated during an increase in mid-level cooling from 4-7 km. It is associated with an increase in the positive A_3 coefficient (dashed line plot in Fig. 5b), but not a decrease in the A_2 coefficient. Figures 2h and i also show the increase in mid-level cooling occurring at the rear of the stratiform region. The thin black lines in Figs. 2h, i show the mid-level rear-to-front flow at the rear of the storm increasing from 6 to 10 m s^{-1}. With the cooling concentrated farther aloft due to the elevated rear inflow jet, an $n = 3$ wave was generated instead of an $n = 2$ wave. It should be noted this $n = 3$ wave is of a different structure than that generated by cooling in the low-levels studied by Lane and Reeder (2001). Because Lane and

Accepted for publication in *Journal of the Atmospheric Sciences*. DOI10.1175/JAS-D-19-0250.1.

Reeder (2001) used a tropical sounding to initialize their simulation, it is likely the microphysical cooling profile was different than that of the mid-latitude convection simulated here.

d. Environmental response

The fast-moving $n = 1$ waves are associated with net decreases in the CAPE field and net increases in the Level of Free Convection (LFC) field (Fig. 6a,b). From Fig. 3a, it is evident that the downward motion portion of the three $n = 1$ wave couplets is stronger than the subsequent upward motion. Because of this imbalance, the CAPE field is reduced by about 500 J kg^{-1} by the associated warming and drying with the first $n = 1$ wave couplet (Fig. 6a), and it does not recover with passage of the updraft portion of the couplets unlike in the study of Su and Zhai (2017). The LFC (Fig. 6b) did not respond as strongly to the $n = 1$ waves. (Note that the CAPE responses that appear in Fig. 6a perpendicular to the $n = 1$ waves, after 60 min and from X=225 to 300 km, are due to isolated cells developing at the right edge of the domain due to model noise and are not caused by wave activity.)

The CAPE field responds to the first $n = 2$ wave generated at 24 min. In the area immediately next to and 10-15 km ahead of the convective line, the CAPE field almost recovers from a minimum of approximately to 870 J kg^{-1} to 1370 J kg^{-1}, near the amount of CAPE in the sounding used for initialization. This result agrees with the simulations of Fovell (2002) that found a "cool/moist tongue" spreading ahead of a squall line, established by lifting associated with an $n = 2$ wave. Shortly after the first $n = 2$ wave, however, a second $n = 1$ wave is generated at 36 min, restricting the recovery of the CAPE field in this same area to no more than approximately 1270 J kg^{-1}. A similar pattern is seen in the LFC field, with the initial $n = 1$ wave increasing the LFC from 1410 to 1530 m within 10-15 km of the convective line, and the subsequent $n = 2$ wave helping the sub-cloud layer not only recover, but further reduce the LFC to approximately

Accepted for publication in *Journal of the Atmospheric Sciences*. DOI10.1175/JAS-D-19-0250.1.

50 m below the value at the start of the simulation. The vertical motion of the $n = 2$ waves is concentrated in the lower half of the troposphere and thus will more strongly affect LFC (compare the vertical structure of the waves in Fig. 2d). Lane and Reeder (2001) noted a similarly stronger response in the LFC field than the CAPE field to higher-order wave modes.

The third slow-moving wave, the $n = 3$ wave, produces a stronger response in the CAPE field, an increase of almost 100 J kg^{-1}, but a neutral to slightly stabilizing effect on the LFC. Again, this would be consistent with a $n = 3$ wave with upward motion in the mid-levels (Fig. 3a) producing adiabatic cooling and a destabilizing influence, yet with downward motion at very low levels warming the subcloud layer and increasing the LFC. The low-level stabilizing influence of this wave is very minimal, however.

The low-frequency waves also modify the horizontal wind field (Fig. 6c). A $n = 1$ wave, for example, should enhance surface level inflow toward the storm and outflow aloft, enhancing westerly shear (e.g., Nicholls 1991, Fig. 5). A $n = 2$ wave should conversely enhance inflow at lower mid-levels, and diminish surface-level inflow, decreasing westerly shear. The first $n = 1$ wave here has a relatively small impact on the 0-5 km shear field due to the arrival of the first $n = 2$ wave shortly thereafter. The first and second $n = 2$ waves, however, in sum reduce the 0-5 km shear by over 7 m s^{-1} due to a combination of decreasing surface inflow by 2 m s^{-1} and increasing 5-km inflow by 5 m s^{-1}. The $n = 3$ wave has a minimal impact.

e. MCS response

Evaluation of parcel trajectories, run using the CM1 parcel trajectory package, reveals air parcels from 0 to 4 km are ingested into the updraft. Storm relative inflow is largely concentrated over the same layer. Thus, modification to that environmental layer ahead of the system will directly modify the air being ingested by the storm, and should affect the system updraft strength. The CAPE

Accepted for publication in *Journal of the Atmospheric Sciences*. DOI10.1175/JAS-D-19-0250.1.

and LFC of the inflow air is taken from the cross-section displayed in Fig. 6a 5 km horizontally ahead of the cold pool. This value and the maximum updraft speed at any level are displayed in Figure 7. The leading edge of the cold pool, for this calculation, was defined as the point where the CAPE field dropped below 200 J kg^{-2}, easily visible as the white area in Fig. 3a; it also corresponds to the location of the -2 K potential temperature perturbation. The variations in CAPE associated with the passage of the first $n = 1$ wave (21 min), first $n = 2$ wave (27 min), second $n = 1$ wave (37 min), and second $n = 2$ wave (55 min) are all visible and marked on Fig. 7b, albeit the response to the second $n = 2$ wave is more subtle. Similar changes are noted in the maximum updraft speed following a short lag as the parcels with modified instability are ingested. For example, following the first decrease in CAPE the peak updraft speed also decreases 7 minutes later; as the CAPE values begin increasing due to the $n = 2$ wave the updraft begins similarly increasing in speed 6 minutes later.

Such correlation appears to indicate the updraft strength and buoyancy of the ingested air are related. A different possibility is cyclical cell development alone, independent of wave activity, is influencing the development of the updraft. Specifically, after development of an updraft, precipitation descends to the surface, creating a cold pool and downdraft that cuts off the storm-relative inflow; as the cold air continues to expand it is able to trigger new convection through the lift on its leading edge (e.g., Weisman and Klemp 1982). In this simulation, however, prior to 70 min the convective updrafts and downdrafts are able to tilt enough that the downdrafts do not cut off the storm-relative inflow (Figs. 8a). Cyclical variations in convective updraft strength are still evident (Fig. 5a), but the convective updraft remains contiguous from the surface to the anvil (Fig. 2). Instead, during that period as precipitation descends to the surface (24 min in Figs. 2c, 5b), a $n = 2$ wave is generated that travels ahead of the convective updraft (located between X=95 and 110 km in Fig. 8b). Through lifting this wave destabilizes the pre-storm layer to such an extent cloud is

Accepted for publication in *Journal of the Atmospheric Sciences*. DOI10.1175/JAS-D-19-0250.1.

able to form (thin black lines in Fig. 8b). The cloud extends 5 km ahead of the convective updraft. The additional latent heat release and buoyancy provided by the condensing water (Fig. 8c) is shortly ingested into the convective updraft, leading to its subsequent intensification (see 34 min in Fig. 5a).

This cyclical behavior of the convective updraft is similar to the cyclical upscale evolution of a convective updraft seen in linear low-frequency wave processes modeled by MNCN97. Examination of parcel trajectories confirms this process. Figure 9 displays parcels whose trajectory culminated inside the convective updraft at (Fig. 9a) 32 min and (Fig. 9b) 42 min. By 42 min parcels flowing through the destabilized region ahead of the convective line from X=95 to 100 km shown in Fig. 8c have reached the convective updraft. In Fig. 9b, lifting and upward motion of the parcels over that same region ahead of the convective updraft is evident, with some parcels reaching speeds upward of 5 m s^{-1} before even being ingested into the convective line. Such lifting is not evident 10 min prior (Fig. 9a), before the destabilizing effects of the $n = 2$ wave. The convective updraft itself also shows higher peak updraft speeds from 2 to 8 km aloft after ingesting this destabilized air (Fig. 9b).

This pattern: increased updraft speed, $n = 1$ wave generation, decreased inflow CAPE, $n = 2$ wave generation, increased inflow CAPE, increased updraft speed, repeats until about 70 minutes into the simulation. At that point both the CAPE field and the environmental response to the waves becomes more muddled. However, at approximately 90 minutes a discrete propagation event occurs (see Fovell et al. 2006, Fig. 16). After passage of the second $n = 2$ wave more small clouds are generated in the newly destabilized air (Figs. 2f-i, 3b) than were generated by the first $n = 2$ wave. These clouds are advected toward the convective line by the ambient wind field. The updraft field is strengthened as it absorbs these smaller updrafts, and a "jump" forward by the convective line occurs at approximately 115 min.

Accepted for publication in *Journal of the Atmospheric Sciences*. DOI10.1175/JAS-D-19-0250.1.

This discrete propagation method appears key to invigorating the updraft and maintaining its intensity at the mature stage of the MCS lifecycle after 70 min. Convective updraft intensity in linear convective systems is frequently related to updraft tilt, as a more strongly tilted updraft is weakened by a downward-directed pressure gradient (Parker 2010). Updraft tilt is typically related to the balance of vorticities generated by the cold pool and low-level environmental storm-relative shear, or the ratio of the cold pool strength, C, to shear (Δu^2_{env}). C is defined by $C^2 = \int_0^h B dz$, where B is buoyancy and h the height at which B reaches 0. B is defined as

$$B = g\left(\frac{\theta - \overline{\theta}}{\overline{\theta}} + 0.61(q_v - \overline{q_v}) - q_t\right) \tag{4}$$

where g is gravitational acceleration, θ potential temperature, q_v water vapor mixing ratio, q_t total hydrometeor mixing ratio, and the bars designate environmental conditions, as in Adams-Selin and Johnson (2013). A ratio of one should lead to an upright updraft, while a number larger than one to an updraft that is tilted rearward over the cold pool (Rotunno et al. 1988; Weisman and Rotunno 2004). Many additional factors have been noted as important to updraft strength beyond low-level vorticity balance, including upper level shear (Coniglio et al. 2006) and the rear inflow jet (Weisman 1992). The $C/\Delta u_{env}$ ratio is used here as a baseline indicator for updraft strength; if the peak updraft speeds increase despite a large ratio, additional factors must be present to explain the updraft strength.

Three different $C^2/\Delta u^2_{env}$ ratio calculation methods are presented in Fig. 7c: the unmodified $\frac{C^2}{\Delta u^2_{env}}$ ratio as described above; a version incorporating the impacts of the rear inflow jet, $\frac{C^2 - u_j^2}{\Delta u^2_{env}}$; and $\frac{C^2}{\Delta u^2_{orig}}$ using the environmental shear at the start of the simulation instead of the wave-modified shear ahead of the convective line. Here, C is the maximum value from anywhere in the cold pool, u_j^2 is defined as $(u_H^2 - u_0^2)$, u_H and u_0 are the storm-relative flow within the system at the height of the cold pool and the surface, and Δu_{env} is the 0-5 km shear in the environment 5 km ahead of

Accepted for publication in *Journal of the Atmospheric Sciences*. DOI10.1175/JAS-D-19-0250.1.

the convective line as defined by the location of the maximum updraft over the lowest 2.5 km. All three $C^2/\Delta u_{env}^2$ values are much larger than one during and after the discrete propagation episode at 90 min due to the strong cold pool and weakened deep-layer shear diminished by the $n = 2$ waves (Fig. 6c). The solid and dashed line calculations of the $C^2/\Delta u_{env}^2$ use u wind speeds from 5 km ahead of the updraft, which were modified by the first $n = 2$ wave after its generation at 24 min. After generation of the second $n = 2$ wave at 52 min, the $C^2/\Delta u_{env}^2$ values continued to increase due to the decreasing shear. The dotted line in Fig. 7c used the shear originally available in the environment at the start of the simulation. Without the modifications of the $n = 2$ waves, $C^2/\Delta u_{env}^2$ would have remained closer to 1, and the downward pressure perturbations acting on the updraft smaller (Parker 2010). However, the increased buoyancy of the inflow air resulting from the lifting provided by the same $n = 2$ waves, in addition to the absorption of smaller convective cells generated by high frequency waves working in conjunction with the $n = 2$ waves, helps to offset that negative effect.

An additional increase in CAPE due to the $n = 3$ wave is evident beginning at 115 min (Figs. 7c, 3a); an increase in updraft speed occurs shortly thereafter starting at 121 min. At that time discrete convective cells formed in advance of the system are also being absorbed. Again, this increase in updraft speed cannot be caused by updraft tilt as all three calculations of $C^2/\Delta u_{env}^2$ have been steadily increasing and should be acting as a depressant on the updraft strength.

4. Shear sensitivities

The control simulation was repeated with three initial sounding perturbations each of CAPE and 0-5 km shear for a total of nine simulations (Table 1). For clarity, this section will focus on the three shear sensitivity tests 14.3H5, 14.3H15 (the control run), and 14.3H25, and the following section

Accepted for publication in *Journal of the Atmospheric Sciences*. DOI10.1175/JAS-D-19-0250.1.

on three instability sensitivity tests, 12.2H15, 14.3H15, and 16.2H15. Comments evaluating the MCS response in all the simulations will be presented at the end.

a. Waves and generating processes

As would be expected, the different initial environments generated MCSs with gross differences, but still some similarities among wave activity. All of the simulations showed an initial increase in mid-level updraft strength (white line plot in top row of Fig. 10) at the same time as a peak in the A_1 coefficient (black line plot in top row of Fig. 10) as the initial convective updraft developed, generating an $n = 1$ wave (solid vertical black lines in top row of Fig. 10). As in the control run, each increase in mid-level latent heating and the A_1 coefficient prior to about 70 minutes into the simulation generates a $n = 1$ wave. While subsequent increases in latent heating potentially also generate $n = 1$ waves, their signal is hidden by higher-order wave modes.

Initially, peak updraft speeds were strongest in 14.3H25 (Fig. 10c). Over time 14.3H15 updrafts (Fig. 10b) reached magnitudes comparable to than those of 14.3H25, while 14.3H5 (Fig. 10a) had weaker updrafts throughout. These results were somewhat different than the trend in peak updraft speeds in squall line simulations with varying shears in Weisman et al. (1988), which observed the strongest initial updraft maxima in simulations with minimal or no shear (their Fig. 3). This difference is likely due to either the different methods of convective initialization used in the simulations, or the depth of the layer of environmental shear. Weisman et al. (1988) used a line of warm bubbles for initialization. With the stronger initial forcing of the dam break used here, strong shears do not have as detrimental an effect on the initial updraft and larger speeds are able to be reached. When the control simulation here was repeated using a line of warm bubbles to initialize convection, initial updraft speeds were not as strong (Fig. 4). However, as simulation time progressed in the shear tests, the strong shear simulations in both this study and Weisman

Accepted for publication in *Journal of the Atmospheric Sciences*. DOI10.1175/JAS-D-19-0250.1.

et al. (1988) produced larger updraft speed maxima. Furthermore, the shear in Weisman et al. (1988) only covered the 0-2.5 km layer instead of the deeper 0-5 km layer as in this study and in Weisman and Klemp (1982), which Coniglio et al. (2004) noted can impact updraft strength.

Latent heating rate trends closely mirrored trends in updraft speed. After the initial peak in updraft speed, the latent heating rates of 14.3H15 and 14.3H25 were fairly comparable. Variations in mid-level updraft strength generally corresponded to similar variations in mid-level latent heating and A_1, associated with $n = 1$ wave generation (Fig. 10a-c). Vertical motions associated with the $n = 1$ waves in 14.3H5 were weaker than those generated in the other two shear tests (e.g., compare Figs. 11a and 12a), coincident with weaker latent heating values.

As precipitation first began to fall below cloud level, latent cooling due to evaporation and melting increased generating $n = 2$ waves during or shortly after minima in A_2 (bottom row of Fig. 10). Horizontal arrows in Figs. 11a and 12a show the new areas of latent cooling that formed when precipitation first reached the surface. Resulting $n = 2$ waves appear in Figs. 11b and 12b (compare with Fig. 2d). As the systems continued to develop, all three developed stratiform regions. The stratiform regions in 14.3H5 and 14.3H15 developed rearward, with increased low-level cooling to the left of the convective updraft (Figs. 11c, 2f); the stratiform region and low-level cooling occurred to the right of the updraft in 14.3H25 (Fig. 12b). Subsequent $n = 2$ waves are evident in all three tests (Figs. 11d, 2d, 12c). No $n = 3$ waves appear in 14.3H5 as latent cooling never expands far above 6 km (Fig. 10d). However, in 14.3H25 and14.3H15, an increase in mid-level cooling appears coincident with development of the mid-level rear inflow jet (Figs. 12d, 2i). This cooling, concentrated in mid-levels and associated with peaks in A_3, generated $n = 3$ waves (Figs. 10f, 12e). (While there are clearly high-frequency waves visible in Fig. 12e, none of them were long-lasting as seen in Fig. 13 and hence are not identified by wave mode.)

Accepted for publication in *Journal of the Atmospheric Sciences*. DOI10.1175/JAS-D-19-0250.1.

The stronger updraft and extra-storm circulation in 14.3H25 lofted more condensate and advected it farther from the updraft, leading to a wider stratiform precipitation region (e.g., compare Figs. 12e and 2g). Much of the extra frozen condensate remained aloft until later in the simulation compared to 14.3H15 and 14.3H5. The cooling rates of 14.3H25 (Fig. 10f) are smaller in magnitude than those of 14.3H15 and 14.3H5 until almost 2 hours into the simulation. In Fig. 13f, the vertical motion signatures associated with the earlier higher order wave modes (i.e., the $n = 2$ waves generated between 20 and 60 minutes) are weaker and less coherent than those seen with later waves (i.e., the $n = 2$ waves generated at 105 and 130 min).

b. Environmental response

As in the control simulation, the initial $n = 1$ wave in all three shear tests corresponds to a decrease in instability as evidenced by the CAPE field (top row in Fig. 14). In 14.3H25 with the strongest initial updraft and $n = 1$ wave response, the CAPE field was reduced to 55% of its original value; the initial perturbations in 14.3H15 and 14.3H5 are each slightly weaker but still evident. The initial $n = 1$ waves also increase the LFC field (middle row in Fig. 14), but perturbation magnitudes are smaller than in the CAPE field. Subsequent $n = 1$ waves in all three tests modify the CAPE and LFC fields only slightly. The initial $n = 1$ wave front can only minimally modify the 0-5 km shear field in all three tests before subsequent $n = 2$ wave arrival (bottom row in Fig. 14).

The upward motion in the lower levels associated with the $n = 2$ waves acts to help the CAPE field within 10-15 km of the convective line partially recover from the stabilizing influence of the $n = 1$ wave (top row Fig. 14). Only in 14.3H15 did the CAPE field return to its value at the start of the simulation. In that case, an $n = 3$ wave with mid-level upward motion was generated by a mid-level cooling perturbation at 100 min (bottom row in Fig. 10). The LFC field, conversely,

Accepted for publication in *Journal of the Atmospheric Sciences*. DOI10.1175/JAS-D-19-0250.1.

was returned to its initial values in all shear tests by the $n = 2$ waves. This result is consistent with $n = 2$ wave vertical motions being more concentrated in the lower layers (i.e., compare the $n = 2$ and $n = 3$ waves in Fig. 12e).

The $n = 2$ wave LFC perturbations are stronger in 14.3H5 and 14.3H15, with only a weak LFC perturbation in 14.3H25. Meanwhile, 14.3H15 and14.3H25 have stronger CAPE perturbations associated with $n = 3$ waves, while 14.3H5 has no evident $n = 3$ waves. The different vertical distributions of cooling in 14.3H5 and 14.3H25 hint at these results. In 14.3H5 cooling was limited to the bottom half of the troposphere (Fig. 11c, Fig. 10c) generating $n = 2$ waves with peak vertical motion in the lower mid-levels (e.g., Fig. 11d). Conversely, the cooling in 14.3H25 was more concentrated in the mid-levels (Fig. 10f), generating $n = 3$ waves with vertical motion more strongly affecting the CAPE field. 14.3H15 exhibited cooling in both vertical locations.

5. Instability sensitivities

a. Waves and generating processes

Simulations with increasing amounts of instability produce larger updraft speeds both during initial development and the mature stage of the simulation (Fig. 15), as would be expected given the results of Weisman and Klemp (1982). Latent heating rates follow a similar trend, with increased heating rates seen in simulations with higher initial instability. As in previous simulations, generation times of the $n = 1$ waves correspond to peaks in the A_1 coefficient and mid-level heating. The vertical motions produced by the $n = 1$ waves at 6 km are stronger and more uniform in the simulations with higher instability (top row, Fig. 16).

Stronger updrafts with increasing instability produced and maintained larger amounts of condensate aloft, resulting in a wider stratiform precipitation region in 16.2H15 compared to 12.2H15 and 14.3H15. For example, compare the total condensate shown in Figs. 17c, 2g, and 18c, each

Accepted for publication in *Journal of the Atmospheric Sciences*. DOI10.1175/JAS-D-19-0250.1.

subfigure shortly after one hour into each of the simulations. Latent cooling rates, particularly over the lower 0-2 km layers, also increased with increasing instability (Fig. 15, bottom row). Higher order wave modes were generated more quickly and more often in higher instability simulations (dashed and dotted lines in bottom row of Fig. 15). As in previous simulations, these wave modes were generated by precipitation descending below cloud level, developing into a stratiform region rearward of the convective line, and development or increase in rear-to-front flow. All these processes occurred more quickly in systems developing in more unstable environments. For example, in 12.2H15, descent of precipitation and latent cooling below cloud level occurs at 38 min (Fig. 17a), followed by an $n = 2$ wave (Fig. 17b). In 16.2H15, precipitation falls below cloud level earlier at 24 min, increasing latent cooling and generating an $n = 2$ wave (Fig. 18a, wave evident in Fig. 18b). Expansion of a stratiform precipitation region rearward in 12.2H15, with associated cooling, occurs at 76 min (Fig. 17c, wave evident in Fig. 17d). In 16.2H15, these processes occur earlier at 62 min (Fig. 18c, $n = 2$ wave in Fig. 18d). The first significant increase in mid-level rear-to-front flow and cooling happens close to the same time in 16.2H15 ($n = 3$ wave also visible in Fig. 18d). Conversely, in 12.2H15 the first $n = 3$ wave isn't generated until 114 min (cooling and wind increase in Fig. 17e, wave evident in Fig. 17f).

b. Environmental response

As seen previously, a decrease in CAPE is associated with each initial $n = 1$ wave (top row in Fig. 19). The strength of the CAPE decrease is directly related to the strength of the $n = 1$ wave response and therefore is strongest in 16.2H15, with the 12.2H15 response being more gradual. Subsequent increases in the CAPE field, again larger in simulations with increasing instability, occur with passage of $n = 2$ and $n = 3$ wave modes. As in the shear tests, the CAPE field was only

Accepted for publication in *Journal of the Atmospheric Sciences*. DOI10.1175/JAS-D-19-0250.1.

returned to its initial simulation value with passage of an $n = 3$ wave with its peak upward motions in the mid-levels.

The impact of $n = 1$ and $n = 2$ waves on the LFC field, conversely, decreases with increasing instability (middle row in Fig. 19). An approximately 250-m increase in LFC associated with the $n = 1$ waves is evident in 12.2H15 with a subsequent $n = 2$ wave-generated decrease of 350 m. In 16.2H15 these perturbations are only about 50 m. The original LFC height in 12.2H15 is near 2 km, closer to the peak vertical velocities in the $n = 2$ waves (e.g., Figs. 17c,d, 18b), explaining the heightened LFC impact in 12.2H5 despite the weaker vertical motions of its waves. That is, the impacts of the $n = 2$ waves on the LFC field depends on both the type of wave and the vertical location of the LFC.

The 0-5 km shear field perturbation strength slightly increases with increasing instability (bottom row in Fig. 19). As in previous tests, only the first $n = 2$ wave has a large impact on the shear field, decreasing it by 5-7 m s^{-1}. This modification to the shear field appears permanent, an important consideration when examining balances among cold pool- and environment-generated vorticities (Rotunno et al. 1988; Weisman et al. 1988) and discussed further in the next section.

6. Sensitivity test impacts on MCS response

As the environment ahead of the MCS is modified by waves, it is expected the strength of the convective updraft will vary in response as was seen with the control simulation. To test this theory, the cross-correlation coefficient between the maximum updraft speed and the surface-based CAPE 5 km ahead of the cold pool edge was calculated for a range of time lags (Fig. 20). This location was chosen to be representative of the storm inflow and is shown for the control run in Fig. 7. The calculations were done for 0-70 and 70-140 min of the simulations separately, as the wave activity generally changes character from cyclical $n = 1, 2$ waves in the first half to chaotic higher-

Accepted for publication in *Journal of the Atmospheric Sciences*. DOI10.1175/JAS-D-19-0250.1.

order wave modes ($n = 2, 3$) in the second half. In the first half of the simulations (Fig. 20a), a strong negative correlation at small positive time lags (<=10 min) is evident, or an increase in updraft speed preceding a decrease in CAPE. That pattern would correspond to an increase in updraft speed and latent heat generating an $n = 1$ wave, decreasing CAPE as it moved ahead of the system. Another significant signal appears in the upper left quadrant of Fig. 20a, corresponding to an increase in CAPE preceding (by a longer time period, about 20-30 min) an increase in updraft speed. This signal appears in all cases except 12.2H5 (blue line), although in 14.3H5 (orange line) the correlation coefficient does not reach the same level of statistical significance. The peak in the upper left quadrant would appear to indicate feedback: as the higher CAPE values are ingested by the updraft it is able to intensify. This process is similar to that shown in Fig. 9. In the second half of the simulations, the correlation coefficient signal changes character and is much less coherent (Fig. 20b). This signal is consistent with the more chaotic nature of multiple low-frequency wave modes being generated. Very little signal shows in the upper left quadrant, indicating that increased CAPE in advance of the system is not correlated with increased updraft speed like it was in the first half of the simulations.

Increases in updraft magnitude in the latter half of the simulations instead were more directly connected with instances of cloud or convective updraft formation ahead of the system, potentially developing into discrete propagation, instead of direct ingestion of higher-CAPE air. Figure 21 displays the cloud water mixing ratio at 2.5 km in addition to the vertical velocity at 6 km, chosen to be representative of the overall updraft strength, for all the sensitivity tests. Formation of cloud ahead of the convective line associated with higher order wave modes appears in the tests with 15 or 25 m s^{-1} shear; the weaker vertical motions associated with higher wave modes in the 5 m s^{-1} shear cases (e.g., Fig. 13d) reduced cloud formation (Fig. 21a-c). In 14.3H15, 16.2H15, 12.2H25, 14.3H25, and 16.2H25, these clouds develop convective updrafts of their own, intensifying the

Accepted for publication in *Journal of the Atmospheric Sciences*. DOI10.1175/JAS-D-19-0250.1.

main updraft when they are eventually advected into it. Discrete propagation events, where the main convective line "jumps" forward when absorbing these new convective cells, are evident in 14.3H15 (around 105 min) and 16.2H15 (around 100 min). Discrete propagation is not necessarily apparent in the higher shear simulations, but due to the leading stratiform nature of these system those events are more difficult to identify. However, updraft intensification following absorption of newly developed convective cells generated by higher-order wave modes is still evident.

7. Discussion and conclusions

A variety of sensitivity studies of MCSs over a range of initial CAPE and shear profiles were conducted in order to examine the different low-frequency gravity wave responses generated during the development and mature stages of the convection. In all simulations, at the time of the initial development of convection a $n = 1$ wave was generated by the increase in mid-level latent heating associated with a developing updraft, agreeing with multiple previous studies (e.g. Nicholls 1991; Mapes 1993; Fovell 2002). The cyclical dissipation and intensification of the convective updraft over the first 60-70 minutes of each simulation produced couplets of $n = 1$ wave responses, similar to the downdraft-updraft couplets simulated by Lane and Zhang (2011) and Adams-Selin and Johnson (2013) and observed by Su and Zhai (2017).

Once precipitation began descending below cloud level, increases in evaporative cooling at low levels generated the first $n = 2$ wave response. As the stratiform precipitation region began to develop rearward and increasing amounts of frozen condensate fell below the melting level, microphysical cooling increased again and another $n = 2$ wave was generated. This pattern occurred in simulations both with trailing and leading stratiform precipitation systems. Finally, during periods of increased development of rear inflow, increased mid-level cooling generated $n = 3$ waves with ascending motion in the mid-levels. The type of higher order wave mode generated ($n = 2$ or

Accepted for publication in *Journal of the Atmospheric Sciences*. DOI10.1175/JAS-D-19-0250.1.

$n = 3$) depended on the vertical location of the cooling, which was determined by its source (e.g., increased stratiform rain or rear inflow). Increased amounts of low-level cooling, and generation of higher order wave modes, occurred more quickly in simulations with larger initial instability.

The impacts to the CAPE, LFC, and 0-5 km shear fields ahead of the MCS followed a fairly similar pattern, albeit of different magnitudes, across all the sensitivity tests. The initial descent associated with the first $n = 1$ wave produced the strongest response in the CAPE field, with the larger CAPE modifications occurring in simulations with larger initial instabilities and thereby stronger vertical motions. While $n = 2$ waves helped the CAPE field recover and decreased the LFC, only passage of $n = 3$ waves increased the CAPE field to its original value. The 0-5 km shear field was weakened by the $n = 2$ waves, reducing the environmental shear field by 5-7 m s^{-1} after their passage. Through the $c/\Delta u$ ratio, it would be expected that the updraft in these simulations would be tilted and weakened due to the reduced shear value (Rotunno et al. 1988; Parker 2010). As that is not the case, additional factors impacting updraft strength are at play.

MNCN97 was able to simulate a similar $n = 1$ couplet response using a linearized model responding to a $n = 1$ heat source multiplied by a sine-squared factor representing sudden intensification and subsequent lessening of the convective updraft (see their Fig. 20d). When they allowed combined $n = 1$ and $n = 2$ heating profiles to increase, decrease, and increase again ("meso-β burst and regrowth" simulation, their Fig. 20i, j) a vertical motion response was produced consisting of a downward-upward motion couplet extending the depth of the troposphere associated with the $n = 1$ signal, followed by cyclical $n = 2$ dipole wave responses. When a slowly increasing proportion of the heating due to the $n = 2$ profile, representing a growing stratiform precipitation region, was introduced to the linear simulation $n = 2$ wave responses were increasingly prominent, particularly closer to the initial heating source due to their slower propagation speeds.

Accepted for publication in *Journal of the Atmospheric Sciences*. DOI10.1175/JAS-D-19-0250.1.

The simulations in this study produced similar responses to those of the linearized model in MNCN97, which is impressive considering the non-linear dynamics of a full convection model. The main difference is the repeated cycles of intensification, dissipation, and regrowth in these simulations produced multiple $n = 1$ downdraft-updraft couplets and $n = 2$ wave response cycles, unlike the single cycle used in MNCN97. The relative impact of the stratiform region on the system heating profile, in addition to increasing with time, also varied depending on the the amount of condensate aloft and hence the environmental instability or shear.

The MCS response to these wave-generated environmental variations, therefore, occurred in two phases: the first, during a time of primarily clear $n = 1$ and $n = 2$ wave generation, showed the updraft speed lagging wave-generated CAPE variations. Similar to the MNCN97 conceptual model, the $n = 2$ wave destabilized the air in advance of the system and as the updraft column ingested more unstable air, the updraft was able to intensify. In the second phase, frequent higher-order wave mode generation made the wave responses less clear. Instead, the higher order wave modes acted as destabilizing forces allowing additional clouds and updrafts to form ahead of the convective updraft and intensify it once advected into it. This mechanism is similar to that of the "cool/moist tongue" described by Fovell et al. (2006), but $n = 3$ wave modes were active as well as $n = 2$ modes in generating the advanced clouds. These additional intensifications can explain why the MCSs in these simulations continued in a mature state despite the reduced 0-5 km shear profiles and unfavorable $c/\Delta u$ ratios. This transition point of 60-70 min, when MCSs shift from cyclical convective updraft development to discrete propagation-style updraft development, occurred after rearward expansion of the stratiform precipitation region and could be considered to occur when the MCS shifts from its developing to its mature stage. Importantly, all these interactions occur in an environment without the necessary trapping levels for bore formation, showing that while bore formation is helpful for nocturnal MCS maintenance, it is not necessary.

Accepted for publication in *Journal of the Atmospheric Sciences*. DOI10.1175/JAS-D-19-0250.1.

Pandya and Durran (1996) and Pandya et al. (2000) found generated low-frequency waves and their associated wind field perturbations highly dependent on the shape of the thermal forcing generating the waves, with the vertical location of the cooling relative to the maximum heating being particularly impactful. They also found that the extra-storm circulation was so highly dependent on the shape of the thermal forcing that variations in the gross large-scale environment had only a small effect when the shape of the thermal forcing was held constant. This study has additionally found that the large-scale environment can modify the types and frequency of generated waves, particularly higher-order wave modes, by modifying the location and amount of condensate aloft and hence the latent heating and cooling profiles. As the generated waves go on to modify the large-scale environment, a closely related feedback loop among these processes is evident. Future work will consider impacts of microphysical perturbations on the MCS thermal forcing shape and magnitude, and therefore on the types of waves generated and their subsequent environmental modifications.

Acknowledgments. This work was supported by National Science Foundation Grant AGS-1636667. High-performance computing support from Cheyenne (doi:10.5065/D6RX99HX) was provided by NCAR's Computational and Information Systems Laboratory, sponsored by the National Science Foundation. All simulation data is archived and available via request. The author also thanks Russ Schumacher for a review of the manuscript, and two anonymous reviewers for their helpful contributions.

References

Adams-Selin, R. D., and R. H. Johnson, 2013: Examination of Gravity Waves Associated with the 13 March 2003 Bow Echo. *Mon. Wea. Rev.*, **141 (11)**, 3735–3756.

Accepted for publication in *Journal of the Atmospheric Sciences*. DOI10.1175/JAS-D-19-0250.1.

Bretherton, C. S., and P. K. Smolarkiewicz, 1989: Gravity waves, compensating subsidence and detrainment around cumulus clouds. *J. Atmos. Sci.*, **46 (6)**, 740–759, doi:10.1175/1520-0469(1989)046⟨0740:GWCSAD⟩2.0.CO;2.

Bryan, G., and J. Fritsch, 2002: A benchmark simulation for moist nonhydrostatic numerical models. *Mon. Wea. Rev.*, **130**, 2917–2928.

Coniglio, M., D. J. Stensrud, and M. B. Richman, 2004: An observational study of derecho-producing convective systems. *Wea. Forecasting*, **19**, 320–337.

Coniglio, M. C., D. J. Stensrud, and L. J. Wicker, 2006: Effects of upper-level shear on the structure and maintenance of strong quasi-linear Mesoscale Convective Systems. *Journal of the Atmospheric Sciences*, **63 (4)**, 1231–1252.

Fovell, R., 2002: Upstream influence of numerically simulated squall-line storms. *Quart. J. Roy. Meteor. Soc.*, **128**, 893–912.

Fovell, R., G. L. Mullendore, and S. Kim, 2006: Discrete propagation in numerically simulated nocturnal squall lines. *Mon. Wea. Rev.*, **134**, 3735–3752.

Gallus, W. A., and R. H. Johnson, 1991: Heat and moisture budgets of an intense midlatitude squall line. *J. Atmos. Sci.*, **48**, 122–146.

Haghi, K. R., D. B. Parsons, and A. Shapiro, 2017: Bores observed during IHOP_2002: The relationship of bores to the nocturnal environment. *Monthly Weather Review*, **145 (10)**, 3929–3946.

Haghi, K. R., and Coauthors, 2019: Bore-ing into nocturnal convection. *Bulletin of the American Meteorological Society*, **100 (6)**, 1103–1121.

Accepted for publication in *Journal of the Atmospheric Sciences*. DOI 10.1175/JAS-D-19-0250.1.

Johnson, A., X. Wang, K. R. Haghi, and D. B. Parsons, 2018: Evaluation of forecasts of a convectively generated bore using an intensively observed case study from pecan. *Monthly Weather Review*, **146 (9)**, 3097–3122.

Koch, S. E., P. B. Dorian, R. Ferrare, S. H. Melfi, W. C. Skillman, and D. Whiteman, 1991: Structure of an internal bore and dissipating gravity current as revealed by raman lidar. *Monthly Weather Review*, **119 (4)**, 857–887.

Lane, T., and M. J. Reeder, 2001: Convectively generated gravity waves and their effect on the cloud environment. *J. Atmos. Sci.*, **58**, 2427–2440.

Lane, T. P., and F. Zhang, 2011: Coupling between gravity waves and tropical convection at mesoscales. *J. Atmos. Sci.*, **68 (11)**, 2582–2598.

Lindzen, R. S., and K.-K. Tung, 1976: Banded convective activity and ducted gravity waves. *Monthly Weather Review*, **104 (12)**, 1602–1617.

Liu, C., and M. W. Moncrieff, 2004: Effects of convectively generated gravity waves and rotation on the organization of convection. *J. Atmos. Sci.*, **61**, 2218–2227.

Mapes, G., 1993: Gregarious tropical convection. *J. Atmos. Sci.*, **50**, 2026–2037.

McAnelly, R., J. Nachamkin, W. Cotton, and M. Nicholls, 1997: Upscale evolution of MCSs: Doppler radar analysis and analytical investigation. *Mon. Wea. Rev.*, **125**, 1083–1109.

Morrison, H., G. Thompson, and V. Tatarskii, 1997: Impact of cloud microphysics on the development of trailing stratiform precipitation in a simulated squall line: Comparison of one- and two-moment schemes. *Mon. Wea. Rev.*, **137**, 991–1007.

Nicholls, M., 1991: A comparison of the results of a two-dimensional numerical simulation of a tropical squall line with observations. *Mon. Wea. Rev.*, **115**, 3055–3077.

Accepted for publication in *Journal of the Atmospheric Sciences*. DOI10.1175/JAS-D-19-0250.1.

Pandya, R., D. Durran, and C. Bretherton, 1993: Comments on "Thermally forced gravity waves in an atmosphere at rest". *J. Atmos. Sci.*, **50**, 4097–4101.

Pandya, R., D. Durran, and M. Weisman, 2000: The influence of convective thermal forcing on the three-dimensional circulation around squall lines. *J. Atmos. Sci.*, **57**, 29–45.

Pandya, R. E., and D. R. Durran, 1996: The influence of convectively generated thermal forcing on the mesoscale circulation around squall lines. *J. Atmos. Sci.*, **53 (20)**, 2924–2951.

Parker, M. D., 2008: Response of simulated squall lines to low-level cooling. *Journal of the Atmospheric Sciences*, **65 (4)**, 1323–1341.

Parker, M. D., 2010: Relationship between system slope and updraft intensity in squall lines. *Mon. Wea. Rev.*, **138 (9)**, 3572–3578.

Parsons, D. B., K. R. Haghi, K. T. Halbert, B. Elmer, and J. Wang, 2019: The potential role of atmospheric bores and gravity waves in the initiation and maintenance of nocturnal convection over the southern great plains. *Journal of the Atmospheric Sciences*, **76 (1)**, 43–68.

Rottman, J. W., and J. E. Simpson, 1989: The formation of internal bores in the atmosphere: A laboratory model. *Quarterly Journal of the Royal Meteorological Society*, **115 (488)**, 941–963.

Rotunno, R., J. B. Klemp, and M. L. Weisman, 1988: A theory for strong, long-lived squall lines. *J. Atmos. Sci.*, **45 (3)**, 463–485.

Shige, S., and T. Satomura, 2001: Westward generation of eastward-moving tropical convective bands in TOGA COARE. *J. Atmos. Sci.*, **58**, 3724–3740.

Stechmann, S., and A. J. Majda, 2009: Gravity waves in shear and implications for organized convection. *J. Atmos. Sci.*, **66**, 2579–2599.

Accepted for publication in *Journal of the Atmospheric Sciences*. DOI10.1175/JAS-D-19-0250.1.

Stephan, C., M. J. Alexander, and J. H. Richter, 2016: Characteristics of gravity waves from convection and implications for their parameterization in global circulation models. *Journal of the Atmospheric Sciences*, **73 (7)**, 2729–2742.

Su, T., and G. Zhai, 2017: The role of convectively generated gravity waves on convective initiation: A case study. *Mon. Wea. Rev.*, **145**, 335–359.

Trapp, R., and J. Woznicki, 2017: Convectively induced stabilizations and subsequent recovery with supercell thunderstorms during the Mesoscale Predictability Experiment (MPEX). *Mon. Wea. Rev.*, **145**, 1739–1754.

Weisman, M., and J. Klemp, 1982: The dependence of numerically simulated convective storms on vertical wind shear and buoyancy. *Mon. Wea. Rev.*, **110**, 504–520.

Weisman, M., J. Klemp, and R. Rotunno, 1988: Structure and evolution of numerically simulated squall lines. *J. Atmos. Sci.*, **45**, 1990–2013.

Weisman, M., W. Skamarock, and J. Klemp, 1997: The resolution dependence of explicitly modeled convective systems. *Mon. Wea. Rev.*, **125**, 527–548.

Weisman, M. L., 1992: The role of convectively generated rear-inflow jets in the evolution of long-lived mesoconvective systems. *Journal of the Atmospheric Sciences*, **49 (19)**, 1826–1847.

Weisman, M. L., and R. Rotunno, 2004: ?a theory for strong long-lived squall lines? revisited. *J. Atmos. Sci.*, **61 (4)**, 361–382.

Wilson, J., S. Trier, D. W. Reif, R. Roberts, and T. M. Weckwerth, 2018: Nocturnal elevated convection initiation of the PECAN 4 July hailstorm. *Mon. Wea. Rev.*, **146**, 243–262.

Accepted for publication in *Journal of the Atmospheric Sciences*. DOI10.1175/JAS-D-19-0250.1.

Zhang, S., D. B. Parsons, and Y. Wang, 2020: Wave disturbances and their role in the maintenance, structure, and evolution of a mesoscale convection system. *Journal of the Atmospheric Sciences*, **77 (1)**, 51–77.

Accepted for publication in *Journal of the Atmospheric Sciences*. DOI 10.1175/JAS-D-19-0250.1.

LIST OF TABLES

Accepted for publication in *Journal of the Atmospheric Sciences*. DOI10.1175/JAS-D-19-0250.1.

TABLE 1. Sensitivity test simulation names.

Simulation name name	Surface q_v (g kg^{-1})	MUCAPE (J kg^{-1})	0-5 km shear (m s^{-1})	Initialization method	PBL
12.2H5	12.2	1519	5	dam break	daytime
14.3H5	14.3	2497	5	dam break	daytime
16.2H5	16.2	3538	5	dam break	daytime
12.2H15	12.2	1519	15	dam break	daytime
14.3H15, CONTROL	14.3	2497	15	dam break	daytime
14.3H15, BUBBLE	14.3	2497	15	warm bubble	daytime
14.3H15, COOL	14.3	2497	15	dam break	nocturnal
16.2H15	16.2	3538	15	dam break	daytime
12.2H25	12.2	1519	25	dam break	daytime
14.3H25	14.3	2497	25	dam break	daytime
16.2H25	16.2	3538	25	dam break	daytime

Accepted for publication in *Journal of the Atmospheric Sciences*. DOI10.1175/JAS-D-19-0250.1.

LIST OF FIGURES

Accepted for publication in *Journal of the Atmospheric Sciences*. DOI10.1175/JAS-D-19-0250.1.

Accepted for publication in *Journal of the Atmospheric Sciences*. DOI10.1175/JAS-D-19-0250.1.

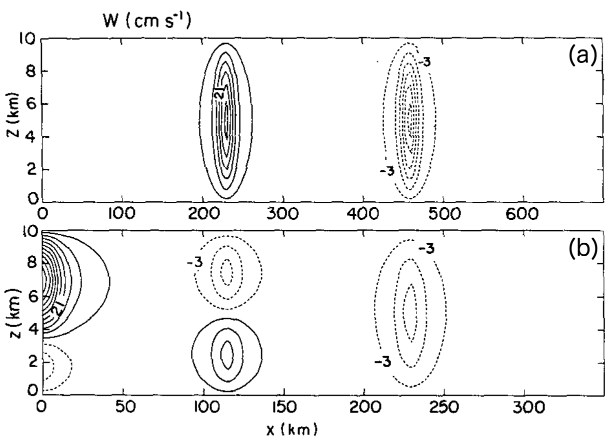

819 FIG. 1. (a) Vertical velocity (3 cm s^{-1}, negative dashed) of a 2.0 J kg^{-1} s^{-1} convective ($n = 1$) heating pulse underneath a rigid lid at 10 km 4 h after start of heating. The heating was turned off after 2 h. Adapted from Figs.10 and 5 of Nicholls (1991).

Accepted for publication in *Journal of the Atmospheric Sciences*. DOI10.1175/JAS-D-19-0250.1.

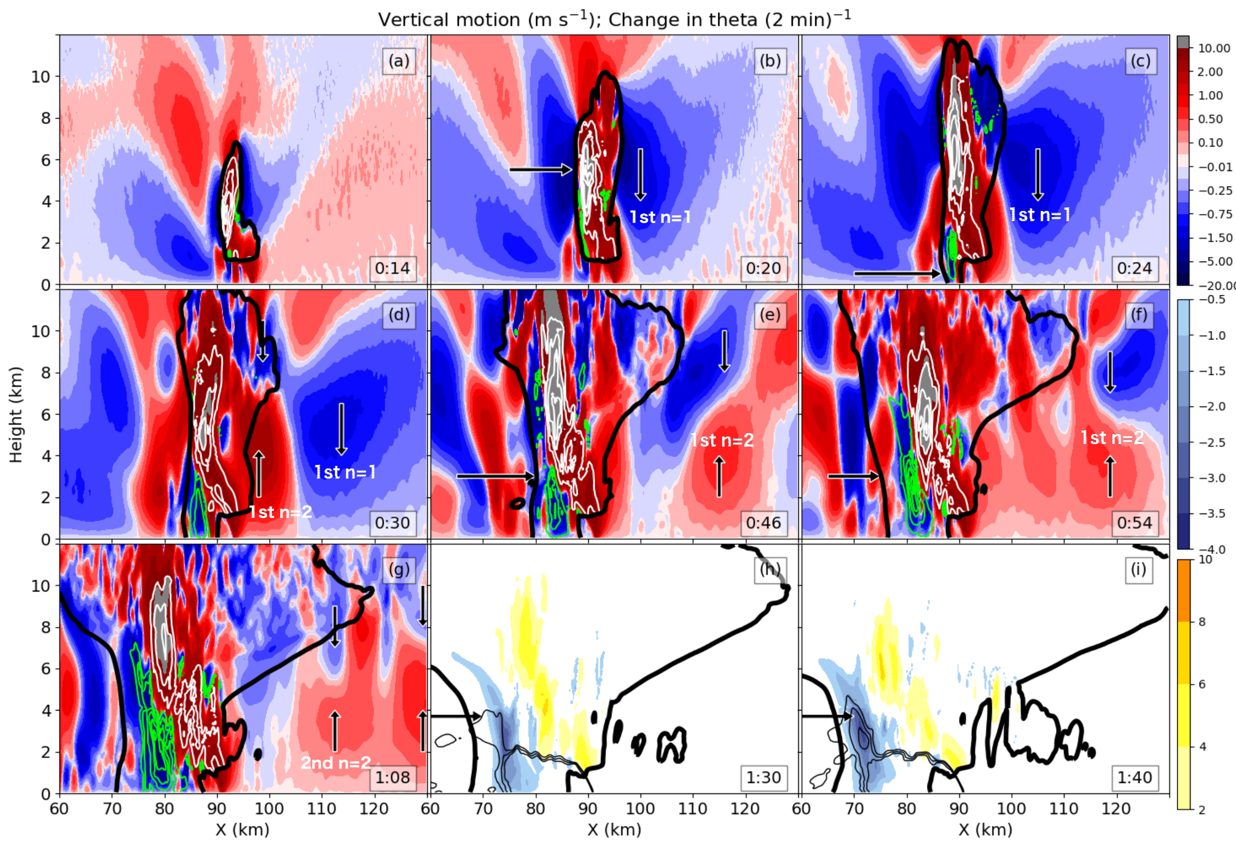

FIG. 2. (a-g) Vertical cross-sections of vertical velocity (color; m s^{-1}), latent cooling (green, 0.5 K (2 min)$^{-1}$), latent warming (white, 2 K (2 min)$^{-1}$), and total condensate (black, 0.1 g kg^{-1}). (h-i) Vertical cross-section of latent warming (yellow shades, 2 K (2 min)$^{-1}$), latent cooling (blue shades, 0.5 K (2 min)$^{-1}$), total condensate (thick black, 0.1 g kg^{-1}), and u wind (thin black, 6, 8, 10 m s^{-1}) from the control simulation (14.3H15). Vertical arrows highlight low frequency waves within the vertical motion field. Horizontal arrows indicate in: (b) increase in mid-level latent heating, (c) increase in low-level latent cooling, (e-f) rearward expansion of the stratiform region, and (h-i) increase in mid-level rear inflow and latent cooling. Simulation time is shown in the lower right corner in each subfigure.

Accepted for publication in *Journal of the Atmospheric Sciences*. DOI10.1175/JAS-D-19-0250.1.

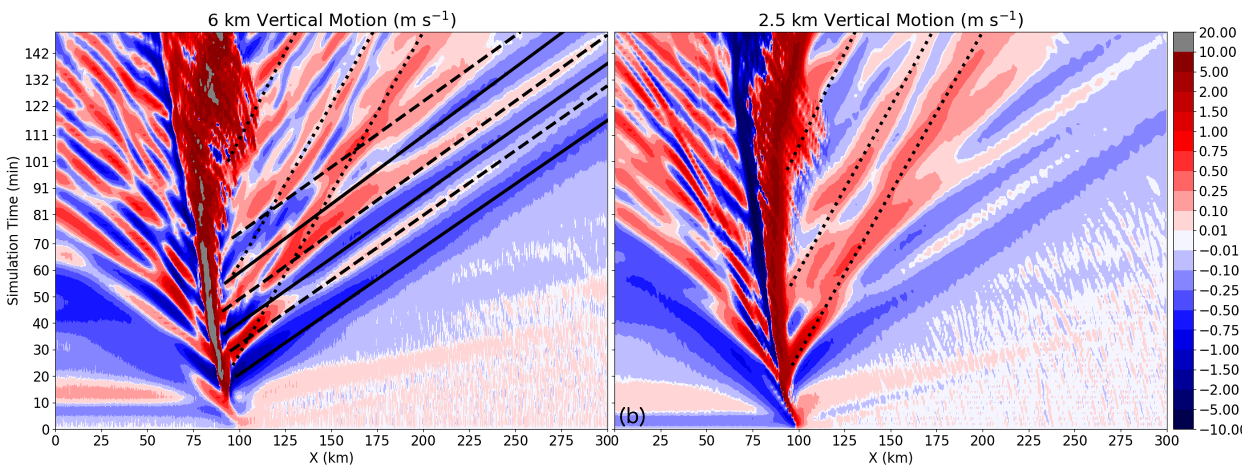

FIG. 3. Hovmöller diagrams displaying vertical motion (m s^{-1}) at (a) 6 km and (b) 2.5 km from the control simulation (14.3H15). X cross-section is averaged 5 km either side of Y=125 km. Three solid lines in (a) delineate three $n = 1$ waves associated with descending motion, and the three dashed lines $n = 1$ waves associated with ascending motion. The dotted lines in both (a) and (b) show three higher order $n = 2$ or $n = 3$ waves.

Accepted for publication in *Journal of the Atmospheric Sciences*. DOI10.1175/JAS-D-19-0250.1.

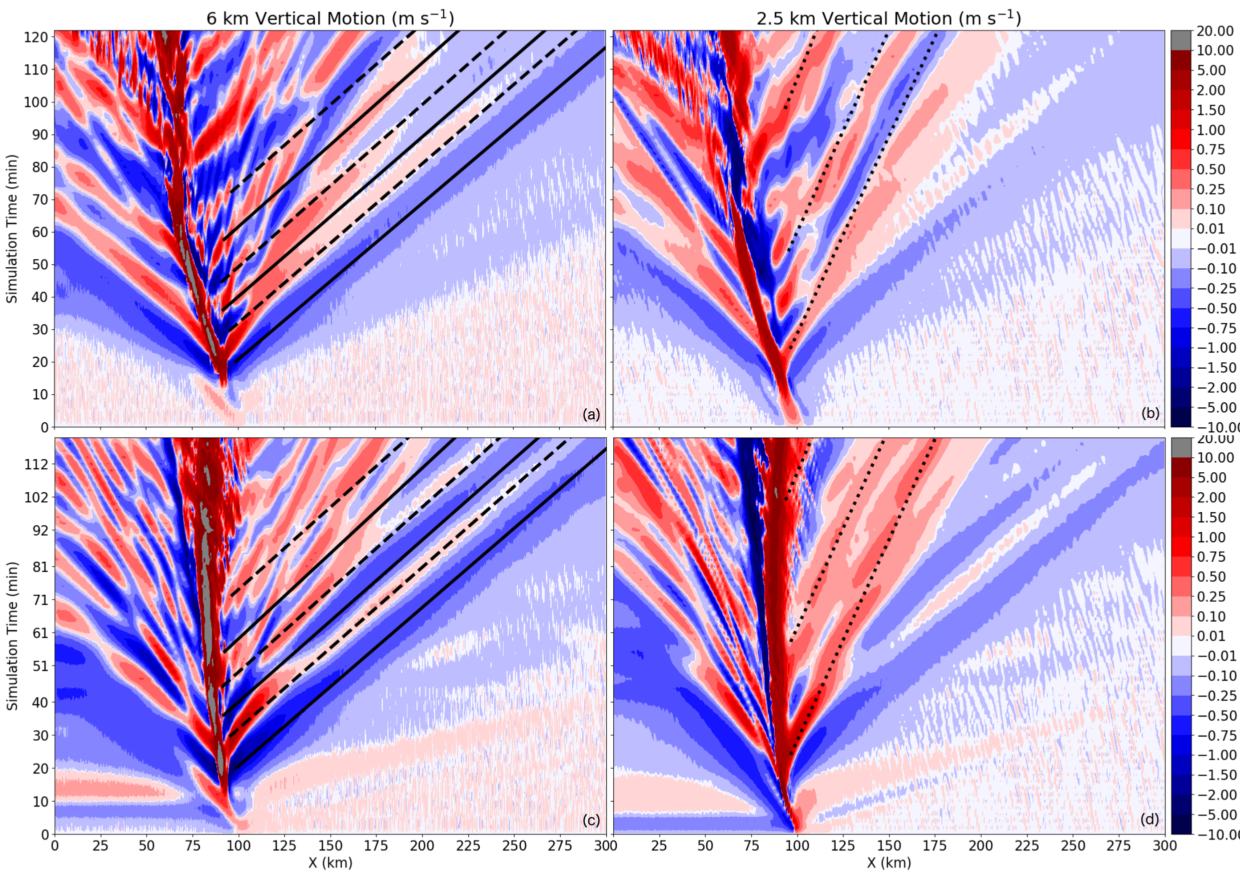

834 FIG. 4. As in Fig. 3, but for (a,b) a warm bubble initialization and (c,d) a simulation with the lowest 1 km
835 cooled as described in the text. Note the solid, dashed, and dotted lines indicating waves are copied from Fig. 3.

Accepted for publication in *Journal of the Atmospheric Sciences*. DOI 10.1175/JAS-D-19-0250.1.

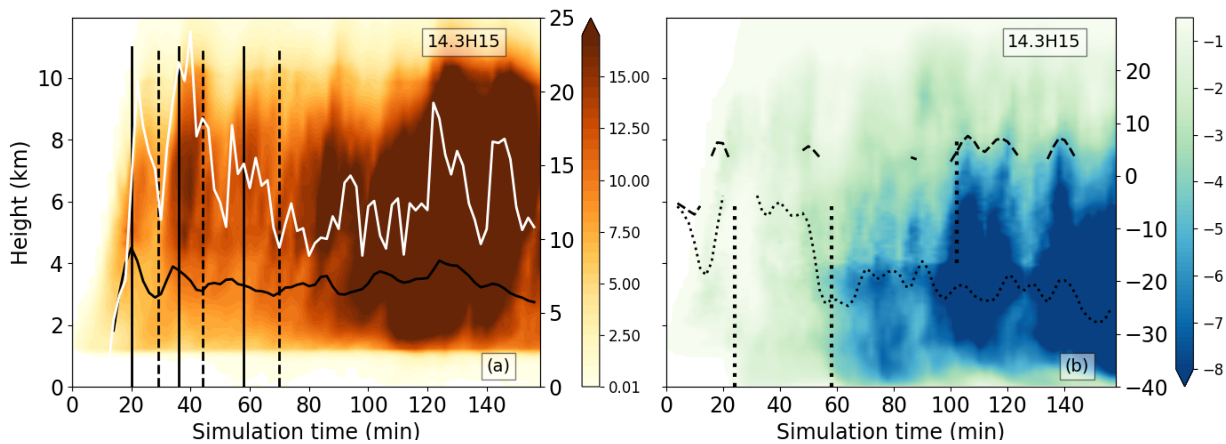

FIG. 5. Time-height diagram showing mean (a) warming and (b) cooling microphysical temperature tendencies (K (2 min)$^{-1}$) over the same X cross-section as Fig. 3 for the control run (14.3H15). Solid, dotted, and dashed vertical lines correspond to start times of the corresponding waves labeled in Fig. 3. The white solid line plot in (a) is the maximum updraft speed within the cross-section at 6 km (m s^{-1}). The black solid line plot in (a) is the coefficient from a Fourier decomposition of the mean heating profile for an $n = 1$ profile; line only shown if the coefficient is determined to be significant per a two-tailed t-test, and the entire decomposition is significant per the F-statistic. The right axis labels in each plot correspond to the values of the coefficients; in (a) they also correspond to updraft speed. Dotted and dashed lines in (b) are the same but for $n = 2$ and $n = 3$ profiles.

Accepted for publication in *Journal of the Atmospheric Sciences*. DOI10.1175/JAS-D-19-0250.1.

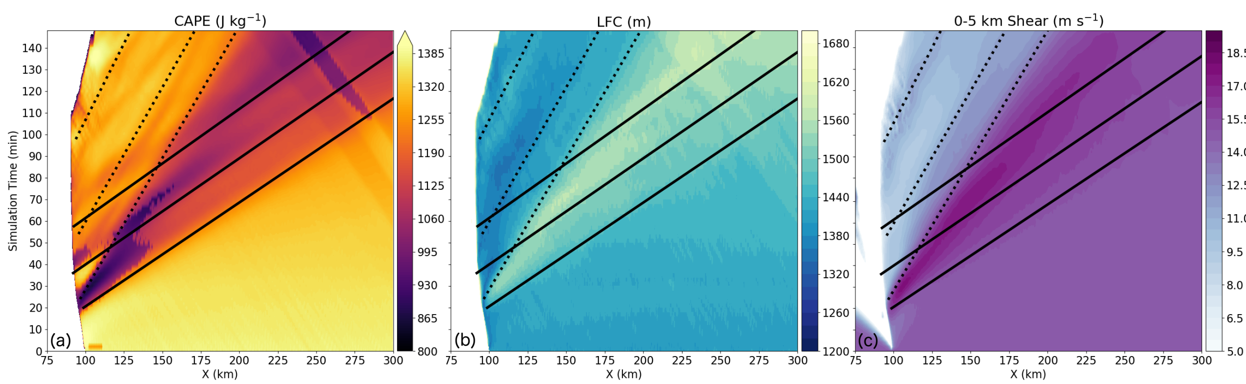

845 FIG. 6. As in Fig. 3, but for surface-based (a) CAPE, (b) LFC, and (c) 0-5 km shear. Upward motion portion
846 of $n = 1$ waves omitted for clarity.

Accepted for publication in *Journal of the Atmospheric Sciences*. DOI10.1175/JAS-D-19-0250.1.

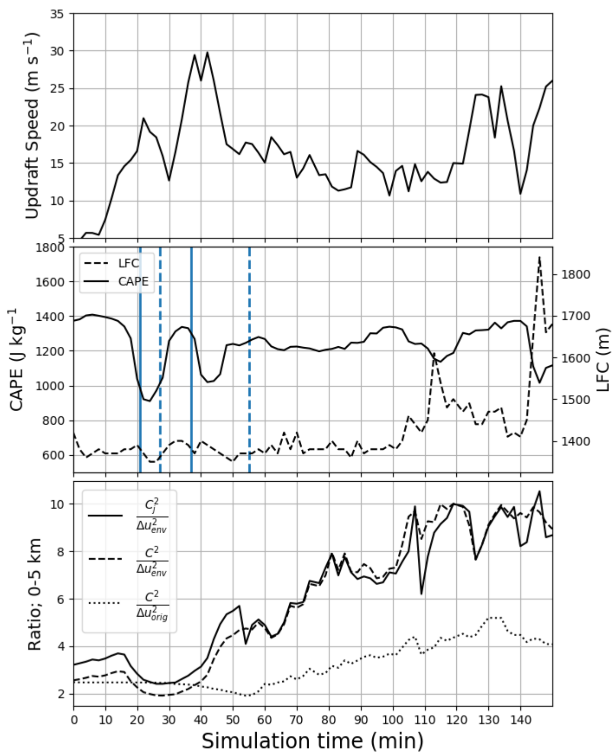

847 FIG. 7. (a) Updraft speed, (b) CAPE and LFC; and (c) the ratio between cold pool intensity and 0-5 km
848 environmental shear. Generation times of four waves are noted in blue ($n = 1$ waves solid, $n = 2$ waves dashed)
849 in (b). In (c) three calculation methods are used as described in the text.

Accepted for publication in *Journal of the Atmospheric Sciences*. DOI10.1175/JAS-D-19-0250.1.

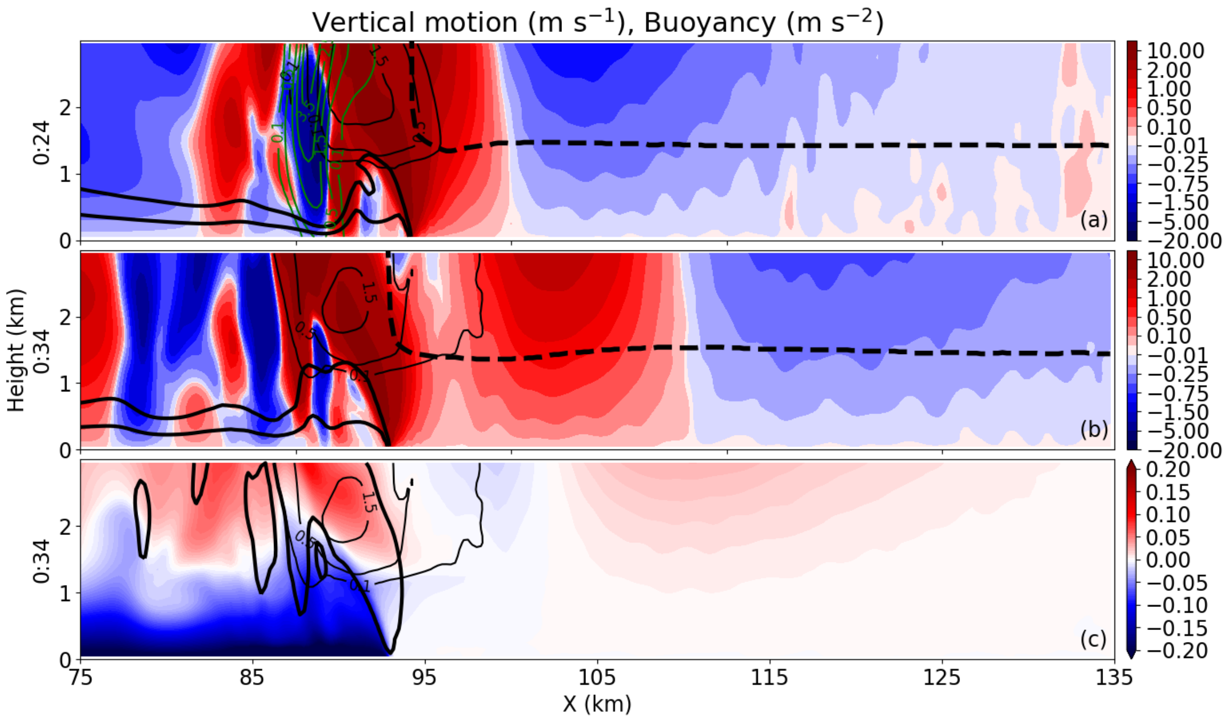

850 FIG. 8. (a, b) Vertical cross-sections of vertical velocity (m s^{-1}) at (a) 0:24 and (b) 0:34 simulation time. Thick black dashed line is the LFC. Thick solid black lines are the -2 and -4K potential temperature perturbations associated with the cold pool. Thin black solid lines correspond to cloud water mixing ratios of 0.1, 0.5, and 1.5 g kg^{-1}. Thin green solid lines in (a) are rain water mixing ratio of 0.1, 0.5, and 1.5 g kg^{-1}. (c) Vertical cross-section of buoyancy (m s^{-2}) from 0:34 simulation time. Thick solid line is vertical velocity of 2 m s^{-1}. Thin solid lines are cloud water mixing ratio as in subfigures (a) and (b).

Accepted for publication in *Journal of the Atmospheric Sciences*. DOI10.1175/JAS-D-19-0250.1.

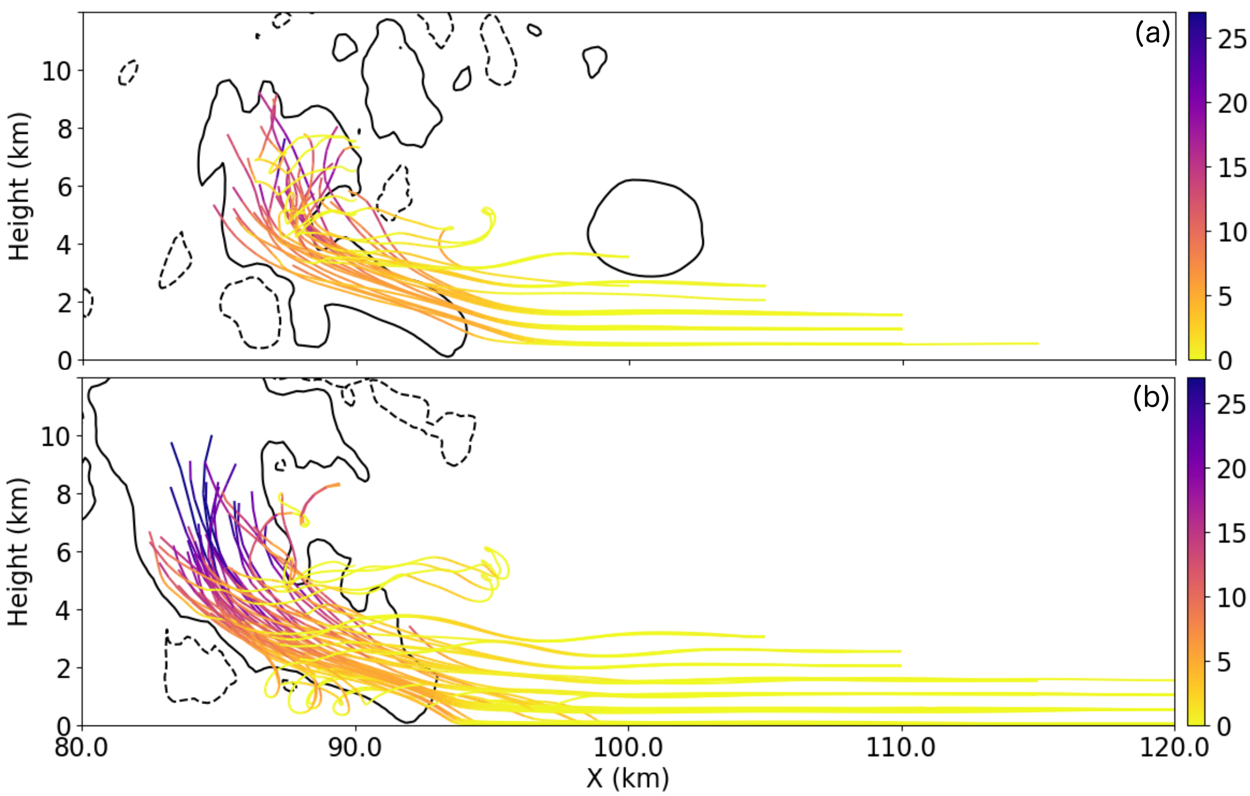

856 FIG. 9. Parcel trajectories from simulation start through (a) 0:32 and (b) 0:42 simulation time for parcels that
857 were in the convective updraft at those respective times . A parcel was determined to be in the convective updraft
858 if it had an upward motion of at least 5 m s^{-1} between 2 and 8 km aloft. Parcel trajectories are color coded by
859 parcel updraft speed (m s^{-1}). The -2 and 2 m s^{-1} vertical motion contours at each time are in black.

Accepted for publication in *Journal of the Atmospheric Sciences*. DOI10.1175/JAS-D-19-0250.1.

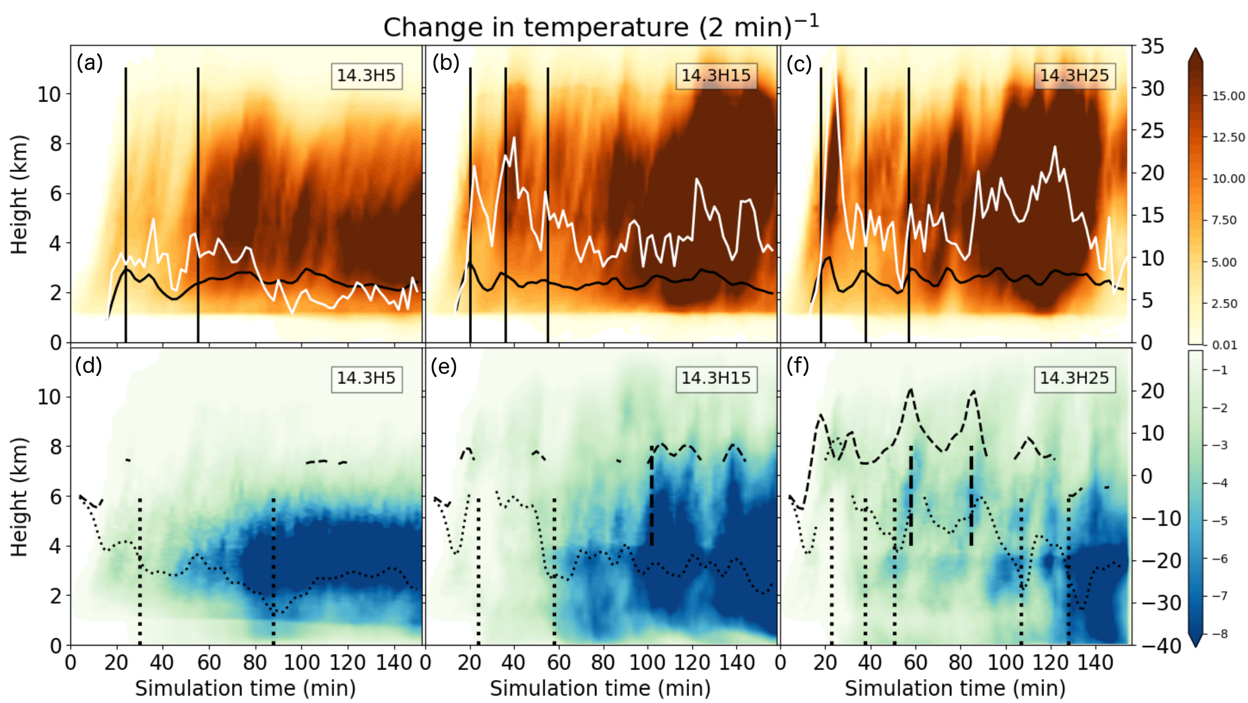

FIG. 10. As in Fig. 5, but for simulations 14.3H5 (a,d), 14.3H15 (b,e), and 14.3H25 (c,f).

Accepted for publication in *Journal of the Atmospheric Sciences*. DOI10.1175/JAS-D-19-0250.1.

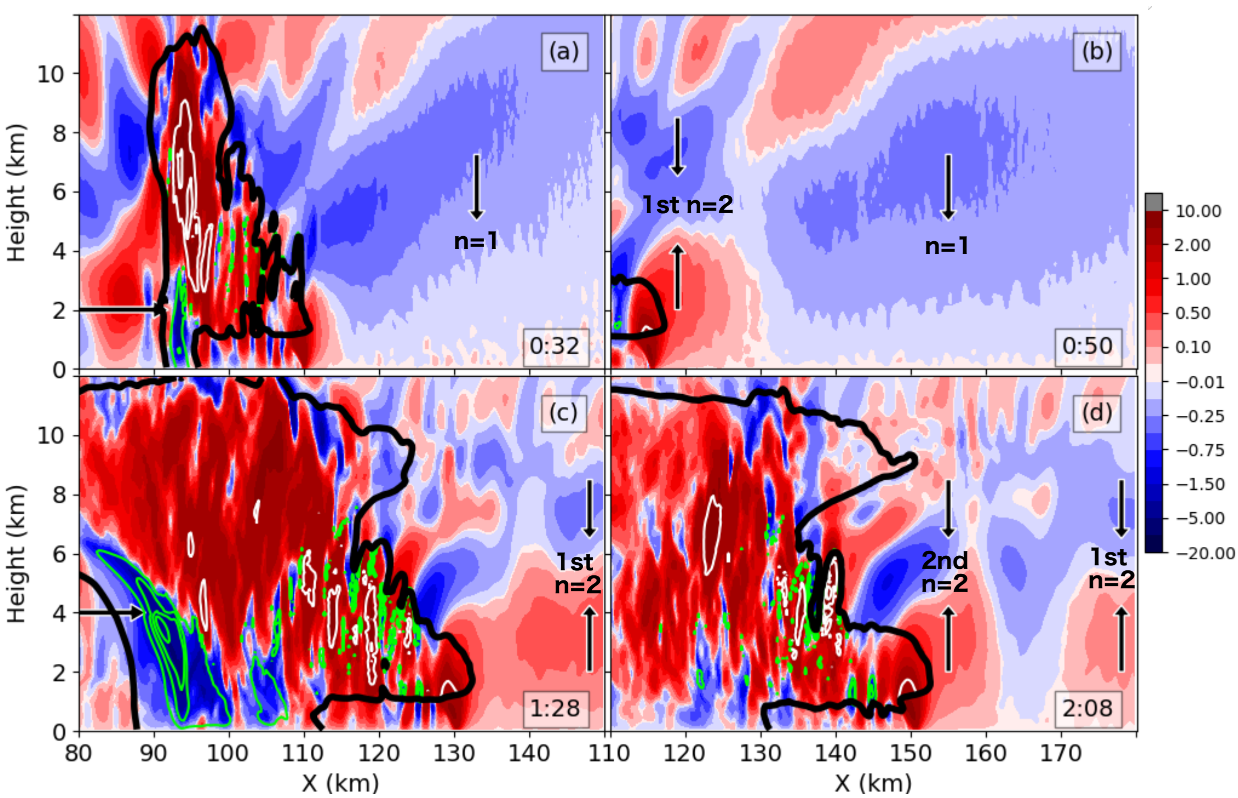

FIG. 11. Vertical cross-sections of vertical velocity, latent heating and cooling, and total condensate as in Fig. 2, but for test 14.3H5. Note the cross-sections in the (b) and (d) are shifted farther ahead of the convective line than in (a) and (c), to capture the wave activity.

Accepted for publication in *Journal of the Atmospheric Sciences*. DOI10.1175/JAS-D-19-0250.1.

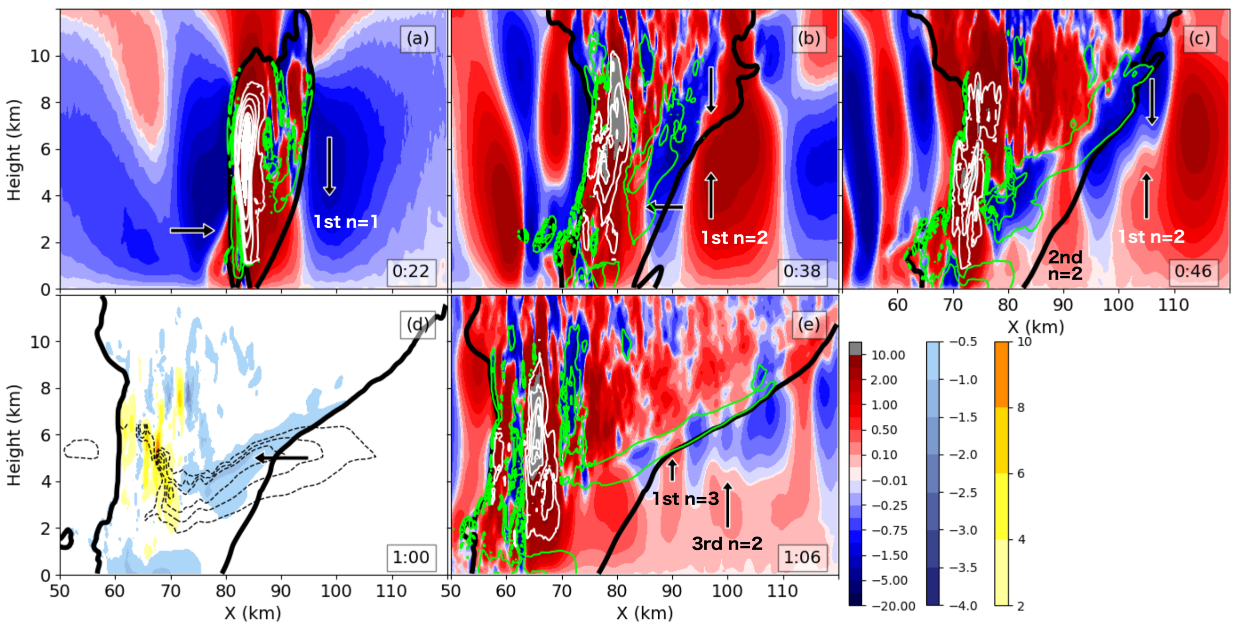

863 FIG. 12. Vertical cross-sections of (a,b,c,e) vertical motion, latent heating and cooling, and total condensate

864 and (d) latent heating and cooling and storm-relative negative u wind as in Fig. 2, but for test14.3H25.

Accepted for publication in *Journal of the Atmospheric Sciences*. DOI 10.1175/JAS-D-19-0250.1.

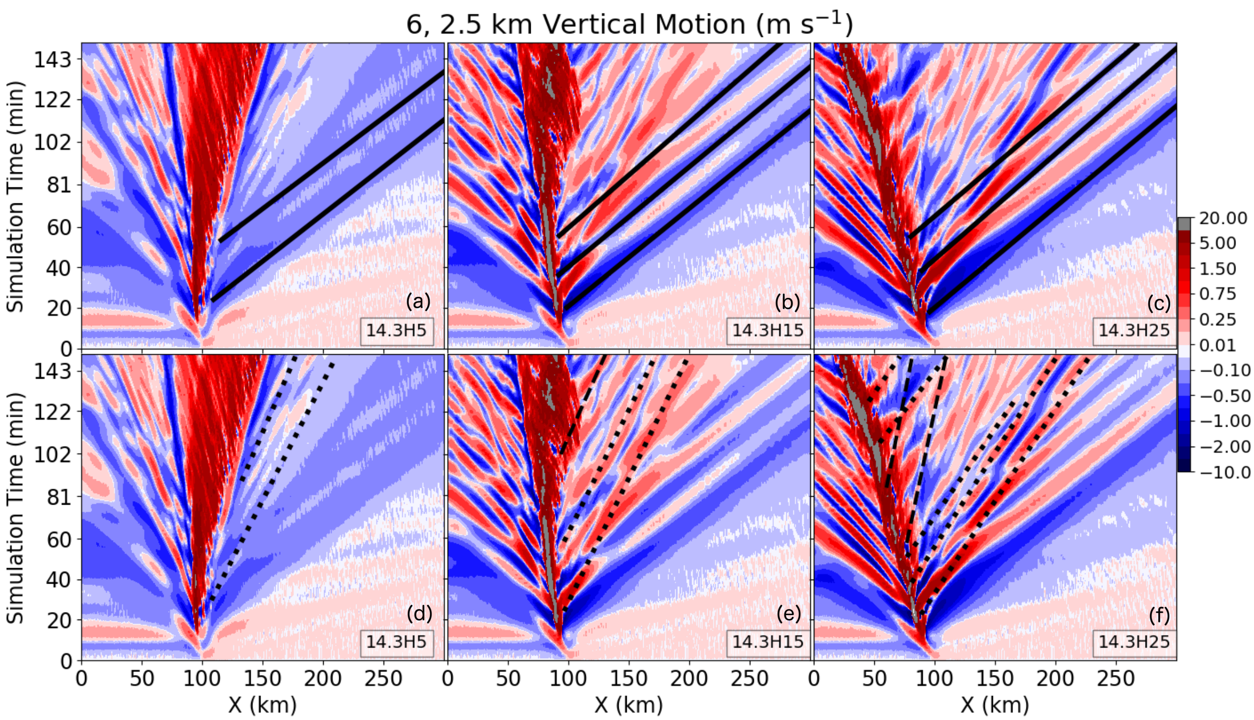

FIG. 13. (Top row) 6-km vertical motion and (bottom row) 2.5-km vertical motion Hovmöller diagrams as in Fig. 3 for three shear sensitivity tests as labeled. In the top row, only the $n = 1$ wave fronts associated with downward vertical motion are labeled.

Accepted for publication in *Journal of the Atmospheric Sciences*. DOI10.1175/JAS-D-19-0250.1.

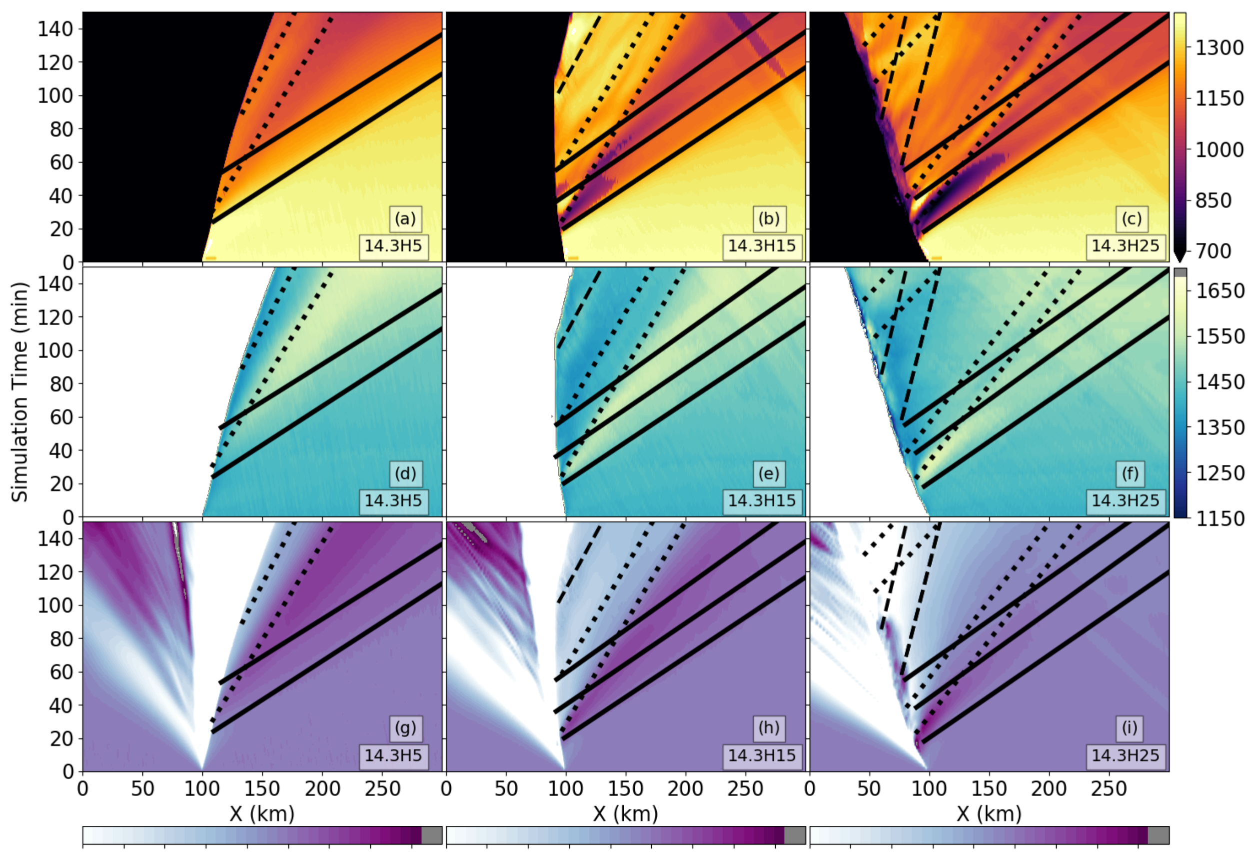

FIG. 14. (Top row) Surface-based CAPE (J kg^{-1}), as in Fig. 6a, for three shear sensitivity tests as labeled. (Middle row) LFC (m) as in Fig. 6b. (Bottom row) 0-5 km shear (m s^{-1}) as in Fig. 6c. Solid, dotted, and dashed lines show the $n = 1$, $n = 2$, and $n = 3$ waves.

Accepted for publication in *Journal of the Atmospheric Sciences*. DOI10.1175/JAS-D-19-0250.1.

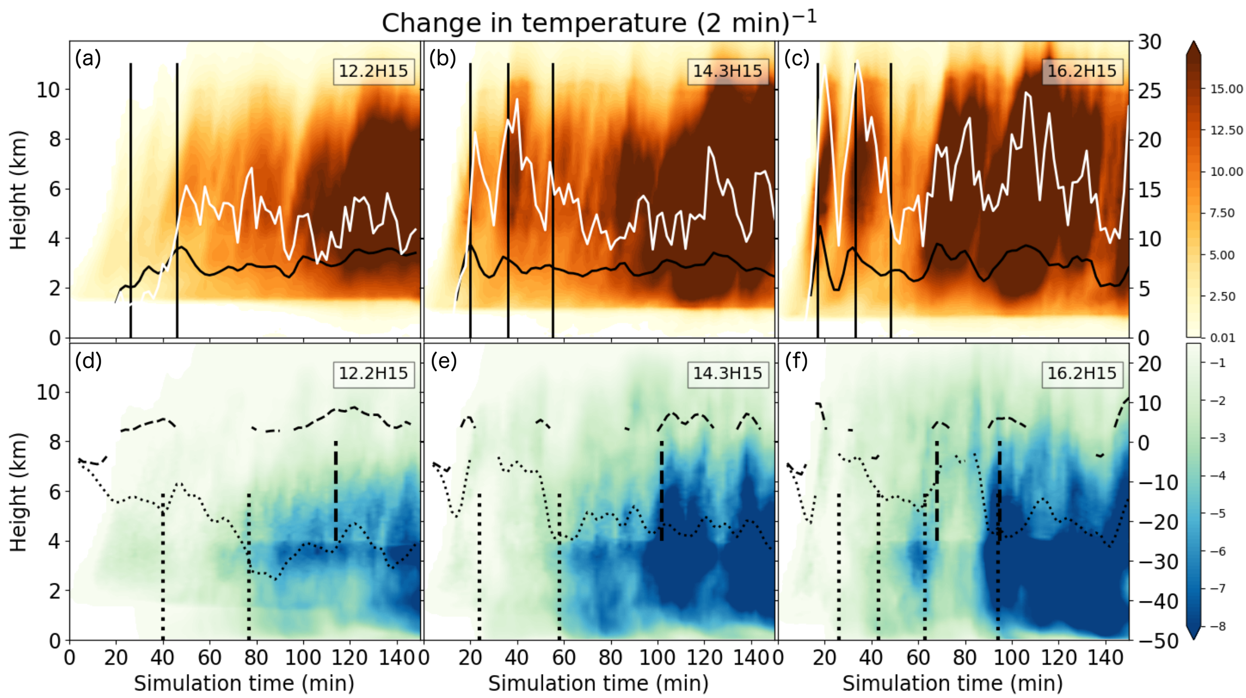

FIG. 15. As in Fig. 10, but for three instability sensitivity tests as labeled.

Accepted for publication in *Journal of the Atmospheric Sciences*. DOI 10.1175/JAS-D-19-0250.1.

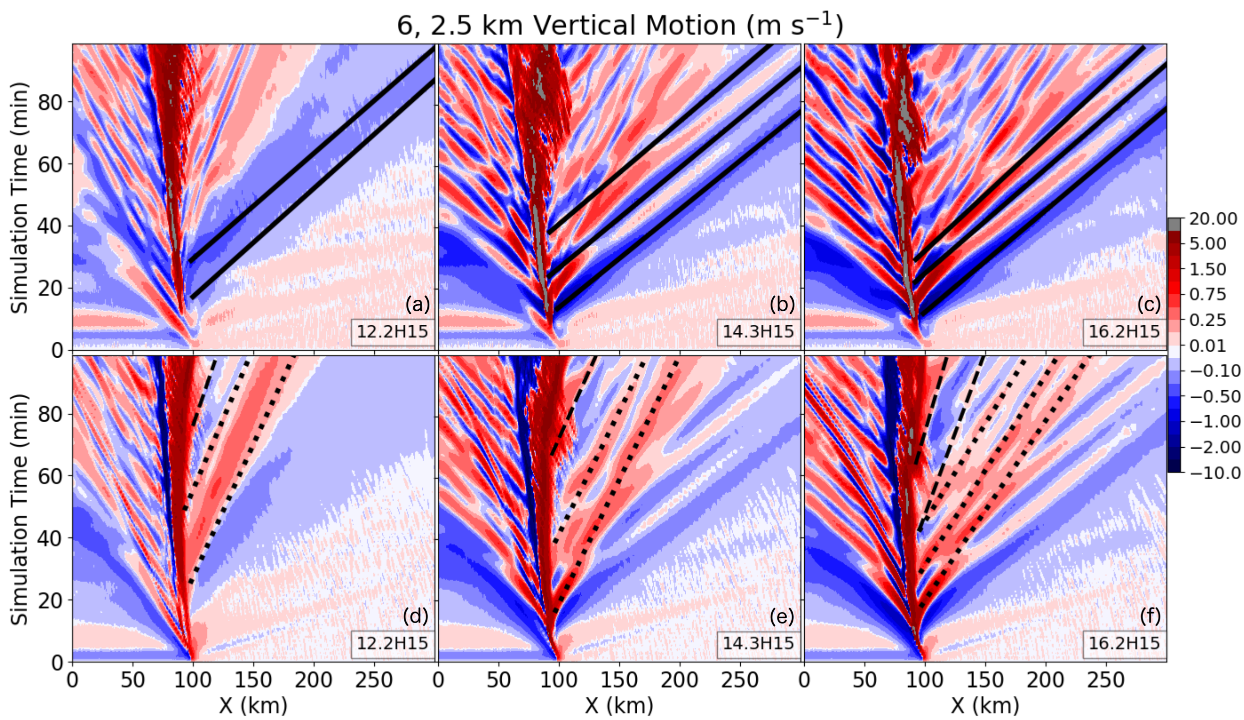

871 FIG. 16. (Top row) 6-km vertical motion and (bottom row) 2.5-km vertical motion Hovmöller diagrams as in
872 Fig. 3 for three instability sensitivity tests as labeled.

Accepted for publication in *Journal of the Atmospheric Sciences*. DOI10.1175/JAS-D-19-0250.1.

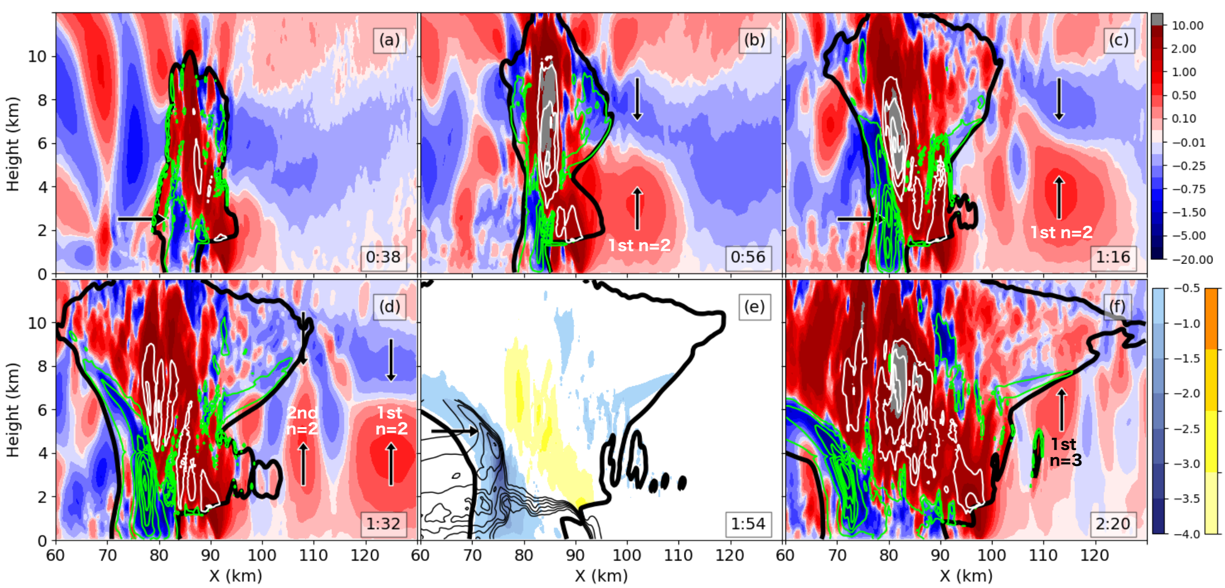

FIG. 17. As in Fig. 2, but for test 12.2H15.

Accepted for publication in *Journal of the Atmospheric Sciences*. DOI10.1175/JAS-D-19-0250.1.

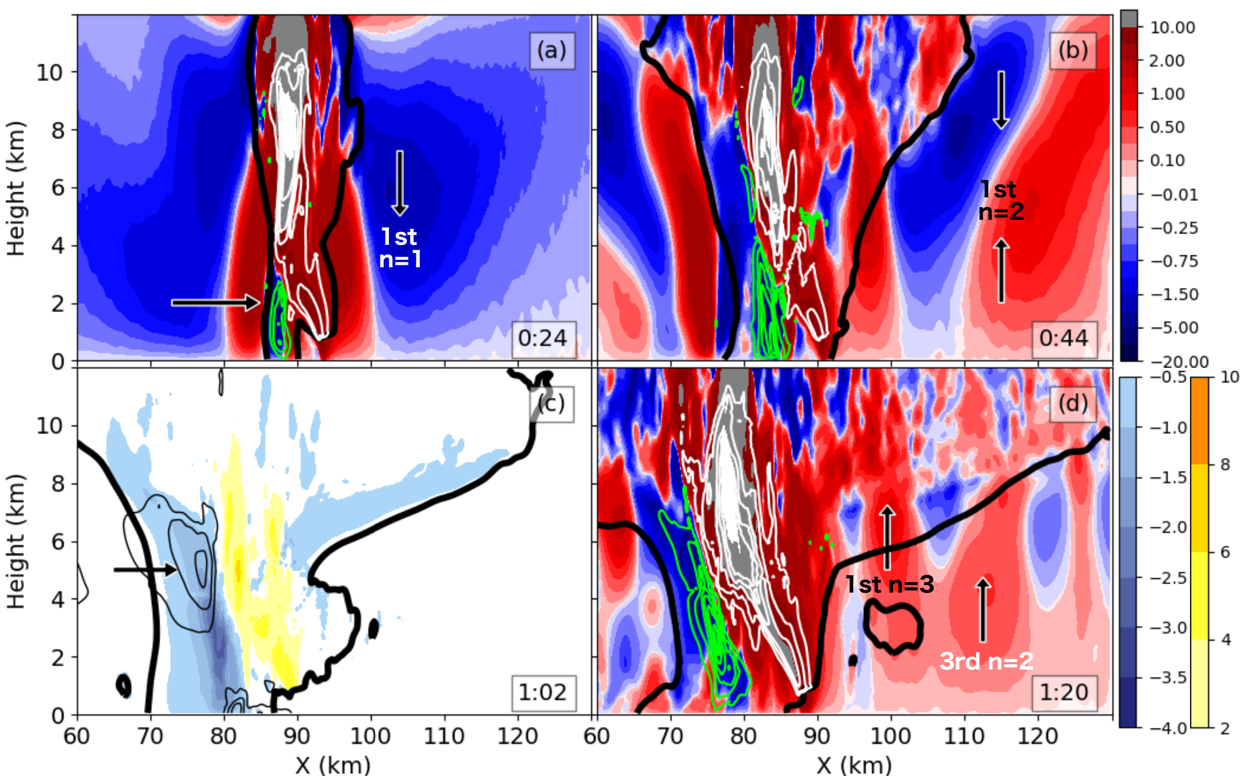

FIG. 18. As in Fig. 2, but for test 16.2H15.

Accepted for publication in *Journal of the Atmospheric Sciences*. DOI 10.1175/JAS-D-19-0250.1.

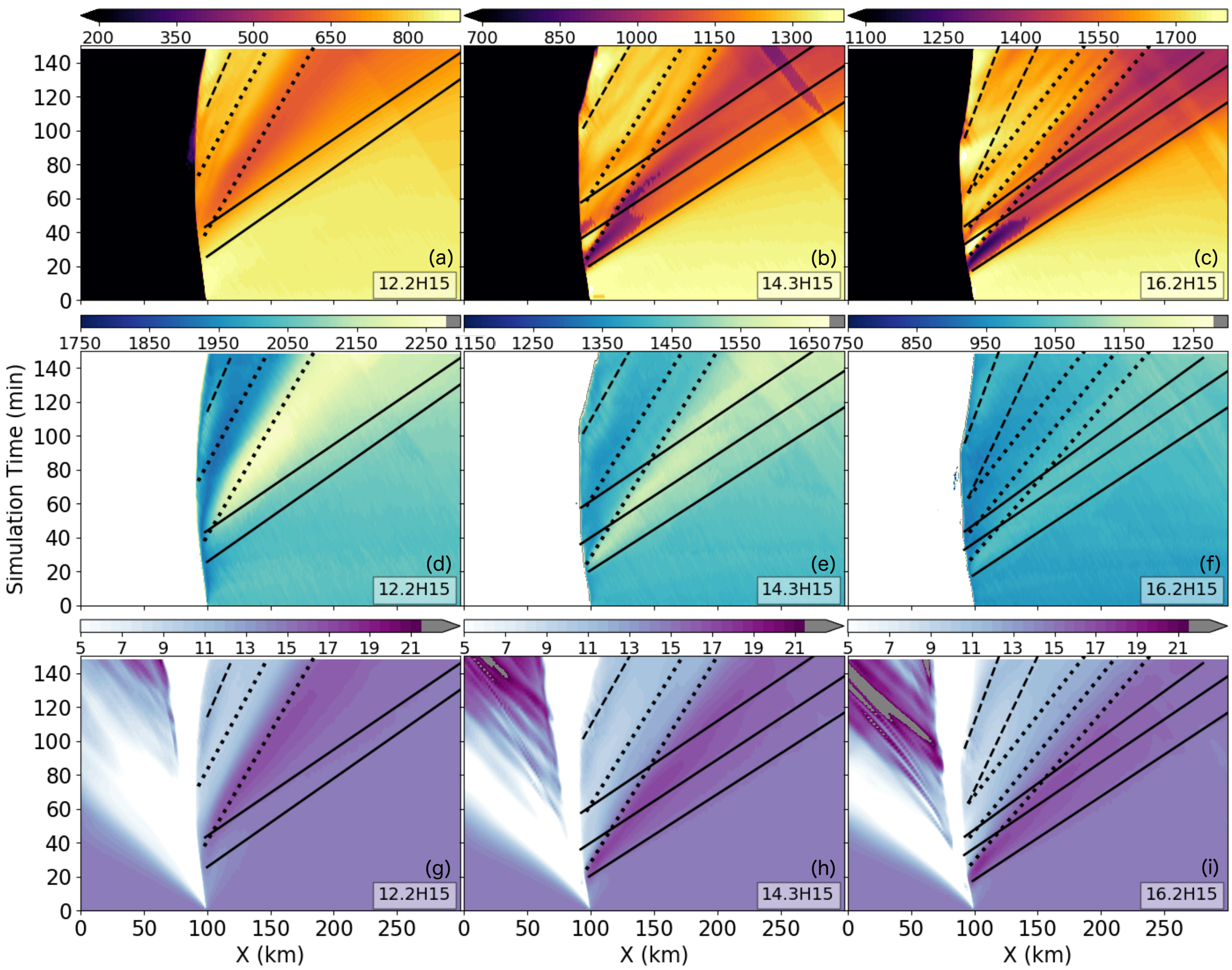

873 FIG. 19. As in Fig. 14, but for three instability sensitivity tests as labeled. Note the maximum and minimum contoured CAPE and LFC values are different for each column, but the total CAPE and LFC ranges covered by each contour set is the same.

Accepted for publication in *Journal of the Atmospheric Sciences*. DOI10.1175/JAS-D-19-0250.1.

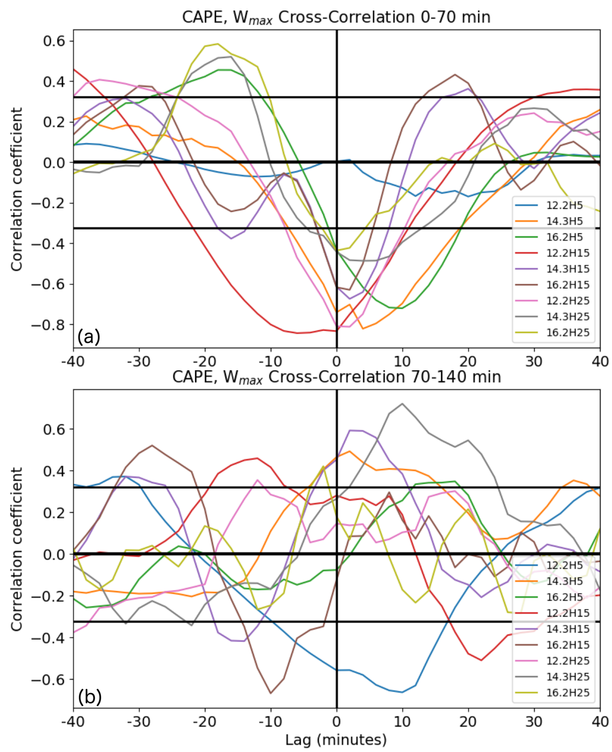

876 FIG. 20. Cross-correlation coefficients for all between surface-based CAPE (J kg^{-1}) 5 km ahead of the cold pool and maximum updraft speed (m s^{-1}) for a range of positive and negative time lags. In a negative time lag an increase in CAPE precedes an increase in maximum updraft speed; in a positive time lag an increase in maximum updraft speed precedes an increase in CAPE. The thick solid horizontal lines delineate coefficients of at least 95% significance, as determined by a two-tailed t-test with over 30 degrees of freedom. (a) Coefficients between 0-70 minutes of the simulation, (b) between 70 and 140 min of the simulation.

Accepted for publication in *Journal of the Atmospheric Sciences*. DOI10.1175/JAS-D-19-0250.1.

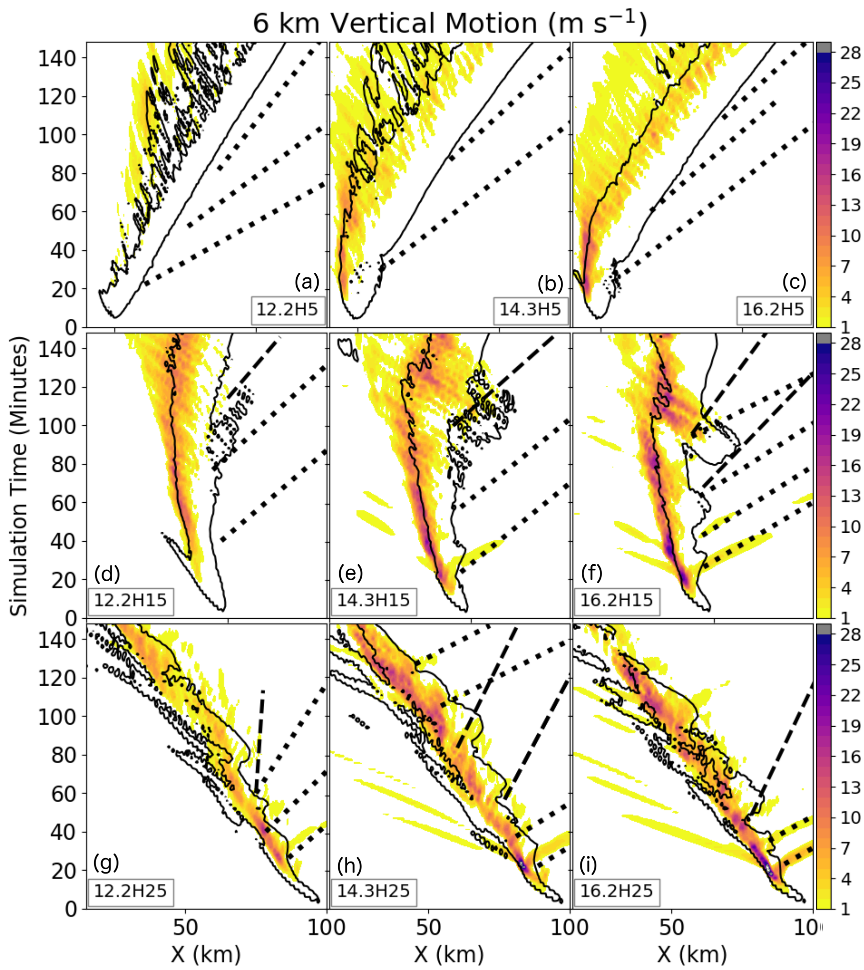

882 FIG. 21. Hovmöller diagrams showing 6-km vertical motion (color fill; m s^{-1}), 2.5-km cloud water mixing
883 ratio (thin black line; 1 g kg^{-1}), and $n = 2,3$ wave modes (black dotted, dashed lines) for all sensitivity tests as
884 labeled.

Accepted for publication in *Journal of the Atmospheric Sciences*. DOI10.1175/JAS-D-19-0250.1.